Physicochemical Characterization of PZT-Based Ultrasonic Transducer Stacks

by

Prudhvi Ram Peri

A Thesis Presented in Partial Fulfillment
of the Requirements for the Degree
Master of Science

Approved July 2018 by the
Graduate Supervisory Committee:

Sandwip K. Dey, Chair
David Smith
Terry Alford

ARIZONA STATE UNIVERSITY

August 2018

ABSTRACT

A piezoelectric transducer, comprised of electroded and active pad PZT layer atop a backing PZT layer and protected with an acoustic matching layer, and operating under a pulse-echo technique for longitudinal ultrasonic imaging, acts as both source and detector.

Ultrasonic transducer stacks (modules), which had failed or passed during pulse-echo sensitivity testing, were received from *Consortium X*. With limited background information on these stacks, the central theme was to determine the origin(s) of failure via the use of thermal and physicochemical characterization techniques.

The optical and scanning electron microscopy revealed that contact electrode layers are discontinuous in all samples, while delaminations between electrodes and pad layer were observed in failed samples. The X-ray diffraction data on the pad PZT revealed an overall c/a ratio of 1.022 ratio and morphotropic boundary composition, with significant variations of the Zr to Ti ratio within a sample and between samples. Electron probe microanalysis confirmed that the overall Zr to Ti ratio of the pad PZT was 52/48, and higher amounts of excess PbO in failed samples, whereas, inductively coupled plasma mass spectrometry revealed the presence of Mn, Al, and Sb (dopants) and presence of Cu (sintering aid) in in this hard (pad) PZT. Additionally, three exothermic peaks during thermal analysis was indicative of incomplete calcination of pad PZT. Moreover, transmission electron microscopy and scanning transmission electron microscopy revealed the presence of parylene at the Ag-pad PZT interface and within the pores of pad PZT (in failed samples subjected to electric fields). This further dilutes the electrical, mechanical, and electromechanical properties of the pad PZT, which in turn detrimentally influences the pulse echo sensitivity.

TABLE OF CONTENTS

LIST OF TABLES

Tables Page

LIST OF FIGURES

Figures Page

Figures Page

CHAPTER 1

INTRODUCTION

The applications of longitudinal ultrasound medical imaging, with varying requirements of piezoelectric transducer sensitivity and spatial resolution of imaging target, span a wide range of frequencies (1-200 MHz). The active piezoelectric transducer, operated under a pulse-echo technique for ultrasonic imaging, acts as both acoustic source and detector of ultrasound. Specifically, the transducer is excited by an electrical signal to project or emit acoustic wave pulses of short duration into a medium to be probed. When such a wave encounters an acoustic impedance mismatch or discontinuity, some of its energy is back reflected as an echo while the rest continues to project (or transmit) forward. When this echo returns to the transducer, a voltage proportional to the acoustic impedance mismatch at the discontinuity is received. The time duration or time-of-flight (TOF) between the projected signal and the returned echo is directly proportional to the distance of the discontinuity from the transducer. Note, the transmitted signal may detect additional impedance discontinuities present at farther distances from the transducer. From the analysis of the time-domain pulse/echo response of a transducer, and the normalized frequency spectrum obtained using the fast Fourier transform, the center frequency, –6 dB bandwidth, insertion loss (characterizing the sensitivity of a transducer in dB via the logarithmic ratio of the peak-to-peak echo and projected voltages; V_{pp}), and focal depth are measured. For example, while spatial resolution can span from 1 mm-50 mm for the corresponding frequency range of 1.5-30 MHz, the higher sensitivity of these devices allows for an increase in penetration depth, higher image signal-to-noise ratio (SNR), and

improved image contrast at higher frequencies. Note, the usable highest frequency for a particular imaging target is constrained by the frequency-dependent attenuation (~ 0.5 dB/cm/MHz) within the body[3]–[6].

Piezoelectric materials of various compositions have been developed for numerous devices in single crystal, polycrystalline ceramic, and composite forms. The important compositions include perovskite structured $BaTiO_3$, tetragonal tungsten bronze-structured lead niobate, ilmenite-structured Li niobate and Li tantalite, perovskite solid solutions of $PbTiO_3$ and $PbZrO_3$ (otherwise known as PZT), Pb-based relaxor piezoelectrics and electrostrictors, piezoelectric copolymers, piezoceramic-polymer composites, and Pb-free compositions[1], [7]–[11].

For medical imaging applications, the PZT family is the most common due to its outstanding electromechanical properties[12]. Note, since pulse/echo transducers operate under thickness mode resonance, the thickness mode coupling coefficient (k_t) is a key metric of efficiency for the conversion of electrical energy into mechanical or acoustic energy (during projection or transmit), as well as from mechanical energy to electrical energy (during receive); k_t values for PZT between 0.45-0.55 is desirable for optimal performance. Additionally, a low planar mode coupling coefficient (k_p) is necessary to limit the excitation of unproductive transverse modes that require expenditure of energy. Moreover, a large relative dielectric permittivity (ε_{33}; free or unclamped) of PZT enables an appropriate electrical impedance match with electronic system circuity, especially for piezoelectric elements with small form factor. Finally, a minimal dissipation factor or dielectric loss tangent ($\tan \delta$) of PZT is desirable to limit the heat generated by the

piezoelectric material during transmit and to improve signal to noise ratio upon echo receive.

One disadvantage of PZT compared to other Pb-based ceramics are their large acoustic impedances. As alluded to before, impedance matching is critical when transmission of acoustic waves (and even other forms of energy) from one medium to another (both from the generator to water medium and from water medium to receiver) occurs. The transfer of incident wave energy from one medium to other results in partial transmission, absorption, and reflection, and the ratio of reflected to transmitted energies is contingent on the characteristic impedances of the two media; note, the transmission is exclusive if these are matched. In the case of acoustic waves the specific acoustic impedance (Z; units in $kgm^{-2}s^{-1}$ or 'Rayl' in honor of Lord Rayleigh) of a medium is given by the product of the density (ρ) and the velocity of sound (υ), i.e., $Z = \rho\upsilon$. For water, since ρ is 1000 kgm^{-3} and υ is 1500 ms^{-1}, Z equals 1.5 Mrayl, and typically for PZT, Z is ~ 30-36 Mrayl. Water and PZT is poorly matched, but the acoustic match between polymers (typically with a Z of ~ 3.5 Mrayl) and water is significantly better[13], [14]. Therefore, in most transducer designs, an active piezoelectric PZT transducer layer atop a backing PZT layer of reduced Z, is protected with a quarter wavelength matching layer that results in acoustic outputs with (a) improved energy transfer efficiency and a short ring down time, and (b) excellent beam sensitivity.

In the current study, 3 mm diameter ultrasound transducer imaging stacks (i.e., modules partially and fully complete) with targeted resonant frequencies between 16-20 MHz were provided to us by Consortium X; an association of companies with expertise in PZT manufacturing, property (mechanical, electrical, electromechanical) characterization,

transducer testing and theoretical analysis, electrical circuit modelling and simulation, and clinical evaluation. Since materials used in commercial transducers, manufacturing processes, device design, and ultrasound performance data are closely guarded trade secrets, Consortium X provided limited and only the following information depicted in items (1)-(4) below:

(1) A fully complete imaging stack was comprised of individual material layers to serve their intended purpose as follows:

(i) thick PZT substrate (or backing) layer to control the backscattering echoes,

(ii) bottom gold contact electrode layer atop the curved backing layer,

(iii) thin PZT pad (or active piezoelectric) layer on gold layer,

(iv) top silver contact electrode layer on the active layer, and

(v) Parylene C polymer (matching) layer with a Z of 2.7 MRayl, interposed between the active piezoelectric PZT pad and water medium, to receive incoming pulse-echo signals.

The broad description of four sets of samples provided by Consortium X for evaluation were as follows:

(a) Stacked layers without the Parylene C coating

(b) Stacked Layers with the Parylene C coating

(c) Complete stack (module) subjected to ultrasonic transducer testing (i.e., subjected to electric fields) and failed (described later)

(d) Complete stack (module) subjected to ultrasonic transducer testing (i.e., subjected to electric fields) but passed

(2) The properties of the PZT substrate (or backing) layer, with very low acoustic impedance and thickness resonance at 2.3 MHz, are tabulated in Table 1. According to Consortium X, this porous layer typically exhibits high thickness coupling coefficient and permittivity. Typical applications of this type of PZT, where the acoustic matching is critical, include broadband medical transducers, broadband non-destructive testing (NDT) transducers, underwater transducers, and low frequency Doppler flow meters.

Table 1. Properties of PZT Substrate (Backing) Layer

Mechanical Properties		
Density		5.7 g/cm^3
Mechanical Quality Factor, Q_m		50
Acoustic impedance, Z_a		18 MRayl
Electrical		
Relative dielectric permittivity (1 kHz), ε_{33}		1150
Dielectric dissipation factor (1 kHz), tan δ		0.15
Curie temperature, T_C		> 350 °C
Electromechanical Properties		
Coupling factors	k_p	0.25
	k_t	0.52
Piezoelectric charge coefficient, d_{33}		340 pC/N
Frequency (thickness) constant, N_t		1170 Hz.m

(3) The properties of the PZT pad (or active) layer, with high Curie temperature, high coupling factors, high mechanical quality factor, low dielectric loss, and purportedly high stability over time, are tabulated in Table 2. The attributes claimed by Consortium X for this dense PZT material are extremely stable performance over several years and highly improved ageing rates, and it could directly replace all other Navy I materials[15]. Typical applications of this type of PZT, where the acoustic matching is

critical, include medical therapeutic transducers, high-power underwater transducers, level sensors, dental cleaners, and hydrophones.

Table 2. Properties of PZT Pad (Active) Layer

Mechanical Properties		
Density		7.7 g/cm^3
Mechanical Quality Factor, Q_m		> 2500
Acoustic impedance, Z_a		> 30 MRayl
Electrical		
Relative dielectric permittivity (1 kHz), ε_{33}		1300
Dielectric dissipation factor (1 kHz), tan δ		0.003
Curie temperature, T_C		> 330 °C
Electromechanical Properties		
Coupling factors	k_p	0.57
	k_t	0.47
Piezoelectric charge coefficient, d_{33}		328 pC/N
Piezoelectric charge coefficient, g_{33}		0.028 V.m/N
Frequency (thickness) constant, N_t		2038 Hz.m

(4) Complete stack (module) subjected to ultrasonic transducer pulse/echo testing (i.e., subjected to electric fields) that resulted in failed module versus passed module. The pulse echo sensitivity characterized by V_{PP} (net) < -26 dB is equivalent to failure. The number of modules failing the original V_{PP} module test has increased over the last few years.

Consequently, the question that has arisen is whether thermal and physicochemical characterization of samples from Consortium X can provide clues as to the origin(s) of failure? Therefore, the objectives of the current work are to:

(A) Identify the individual layers of the multi-layered transducer stack; composition and thickness

(B) Determine the phase, microstructure, dopants and defects in the active pad PZT, and to ascertain their consistency in various samples

(C) Determine whether microstructural observations and alterations are manufacturing process induced or driving electrical field induced, and whether they can be related to the observed failure

The challenges to accomplish the stem from the lack of complete information (proprietary to Consortium X) on materials and processing methods, and unbeknown to us of whether the current sets of samples received from Consortium X conform to the typical properties claimed by Consortium X and depicted in Tables A & B.

CHAPTER 2

LITERATURE REVIEW

2.1 PZT Material:

A material can be called a piezoelectric solid if it develops electric charge when under mechanical stress. This is called direct piezoelectric effect. The inverse piezoelectric effect is when the material changes its shape in reaction to a voltage being applied across it. The direct piezoelectric effect causes net dipoles to align together resulting in polarization or electric charge. For a material to be piezoelectric, it cannot have a center of symmetry as the symmetry always leads to zero net dipoles. Out of the 32 crystal classes, only 20 classes exhibit lack of center of symmetry. The most widely used piezoelectric ceramic is PZT because of its excellent properties and low cost[16].

PZT has a perovskite type crystalline structure with typical formula ABO_3 and is a solid solution of $PbTiO_3$ and $PbZrO_3$. The crystal structure is a cubic unit cell with a large divalent cation (A) on the corners, a smaller anion (B) in the body center and oxygens in the face centers [1][17].

At room temperature if the Ti content is higher ($X<0.45$), then the unit cell has a tetragonal structure and if the Zr is higher ($X>0.49$), then the unit cell has a rhombohedral structure. From the Figure 1, the boundary between the tetragonal and rhombohedral structures is referred to as morphotropic phase boundary or MPB. This MPB boundary composition has been intensely studied and is appealing to the PZT industry since it exhibits enhanced piezoelectric properties[1][18].

According to Figure 1, the phase diagram of PZT shows that above the Curie temperature the material has a cubic structure. This structure is centrosymmetric which

means no net dipoles are present, hence no polarization. The material below Curie temperature is tetragonal in crystal structure and therefore has a net electric dipole. These dipoles can switch directions by applications of an electric field; this behavior is termed ferroelectric. They give a net dipole moment for a given domain and, in turn, a net polarization. By applying a strong electric field at slightly below Curie temperature, the domains align with the field in a process called poling. After removing the field, the dipoles remain locked, giving the PZT a net polarization and deformation. [1], [16].

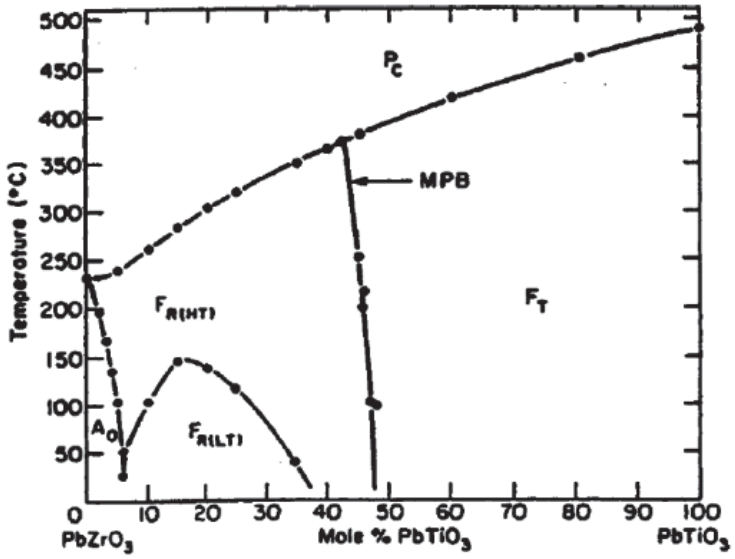

Figure 1. PZT Phase diagram[1].

2.2 Dopants:

Doping is performed to improve the properties of PZT. Different dopants effect the properties differently. Isovalent additives on A/B sites such as Sr, Ca, Ba (for Pb) and Sn (for Zr or Ti); shifts Tc. Donor additives on A/B sites such as trivalent La, Bi, Nd (for Pb), & pentavalent Nb, Ta, and Sb (for Zr and Ti). Acceptor additives on A/B sites such as monovalent K, Rb (for Pb), & trivalent Co, Fe, Sc, Ga, Cr, Al, Mn, (for Zr and Ti). Donor

dopants are high valence cations which induce cation vacancy and causes easy domain wall motion. The PZT's doped with donor dopants are called soft PZTs. Acceptor dopants are lower valence cations which induce oxygen vacancy and causes domain wall motion to be difficult. The PZT's doped with acceptor dopants are called hard PZTs.

Table 3. Effects of Dopants

Donor Doped		Acceptor Doped
Yes	Modify Extrinsic Response	Yes
Larger	Domain Wall Contributions	Smaller
Facilitates (Soft)	Domain Wall Motion	Inhibits (Hard)
Lower	Piezoelectric constant d_{33}	High
High	Mechanical Quality Factor, Q_m	Low
Reduced	Dielectric loss	Relatively high

2.3 Microstructure:

Yang et al. studied effects of microstructure on piezoelectric properties for PZT. Porosity and grain size influences piezoelectric properties significantly. It is mentioned that porosity is decreased as sintering temperature is increased (due to densification) which increases the dielectric constant. Also as the grain size increases, the domains have large area of movement which improves piezoelectric coefficients. Also, reduction in porosity improves the piezoelectric properties. It is noted that relative dielectric constant decreases with increasing porosity and piezoelectric constant increases with increasing grain size. Accumulation of porosity clusters causes areas within ceramic which does not contribute to piezoelectric properties.

2.4 Composition:

The MPB is the division between tetragonal and rhombohedral ferroelectric phases. Tetragonal phase has higher Ti content and rhombohedral phase has higher Zr content. The MPB at room temperature is at 52/48 (Zr/Ti) ratio. The high curie temperatures lead to stable ferroelectric phases in the PZT ceramics and the MPB two phase region has higher piezoelectric properties than other compositions. This is due to availability of higher number of orientation states that can be realized. Any variation in Zr/Ti ratio can also lead to change in piezoelectric properties.

2.5 Transducer Stacking:

The wide ranged applications of transducers such as medical ultrasound imaging, sonars, nondestructive material testing etc. are based on one single principle called ultrasonic echo field[19]. The conversion of electrical energy into mechanical for generation of acoustic pulse and then conversion of received echo in mechanical energy to electrical energy is called ultrasonic echo field[20]. The transducer creates images in real time from the received echoes because their intensities reflect the target material.

A general stacking of a transducer includes protection layer, matching layers, piezoelectric material (pad PZT) and backing layers. The matching layers are used to improve signal transmissions and it's not uncommon to use multiple matching layers. The backing layer is used to damp the reflecting waves to avoid it from effecting echo pulse[21]–[23]. PZT based transducers are widely used owing to its good piezoelectric properties and affordability. The commonly used protection layer for transducers is Parylene.

The piezoelectric properties that influence the transducer working and its signal quality are acoustic impedance matching, electromechanical coupling coefficient, and electrical impedance matching[19]. The protective matching layers are selected such that their acoustic impedance matches with that of the medium, and generally the backing layers are composed of piezoelectric material with low acoustic impedance compared to the active layer[22].

2. Manufacturing Procedure[2], [21], [22], [24], [25]:

Figure 2 shows the pad printing of piezoelectric material. Pad printing is a fast, cheap and versatile process to prepare high quality PZT thick films with curvature. The paste used for pad printing is prepared by regular mixed-oxide method and sintering of the paste is performed after pad printing. The pad printing consists of a silicone rubber pad, steel cliché, a scalpel, and a substrate. The steel cliché has PZT paste which is attached to the silicon rubber pad. The scalpel is used to remove excess paste. The rubber pad is pressed on to the substrate to deposit or print paste. It takes multiple pressings to achieve desired thickness of pad PZT. The substrate is removed by oven drying at around 100ºC. Then pad PZT is sintered for 1 hour at 850-900ºC. The top and bottom surface of pad PZT are printed with silver and gold electrodes respectively. The samples are treated in hot oil and then poled in air at around 150ºC. The applied field and time of poling depends on the type of material used for pad PZT. The substrate used in this process is generally a PZT material like pad PZT, which acts as the backing layer for the transducer. Given the similar compositions, the substrate and pad PZT have similar acoustic impedance and sintering behaviors. The substrate PZT doesn’t contain any dopants unlike pad PZT, to reduce the

cost of transducers. Given the flexibility of pad printing, even the thick films can be deposited on curved surfaces without cracks.

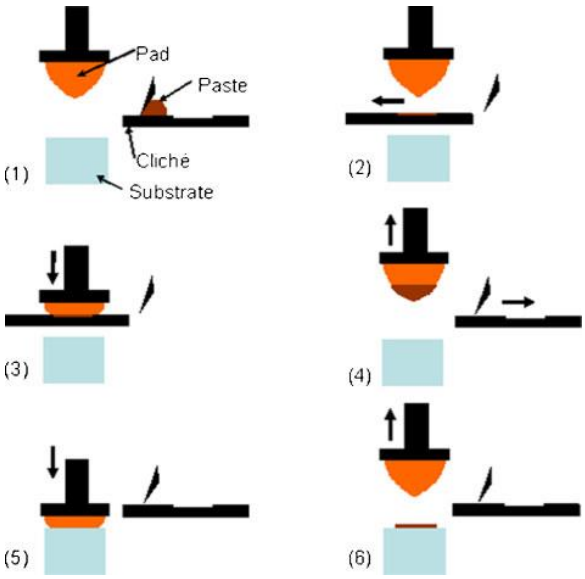

Figure 2. Pad printing of piezoelectric material on substrate[2].

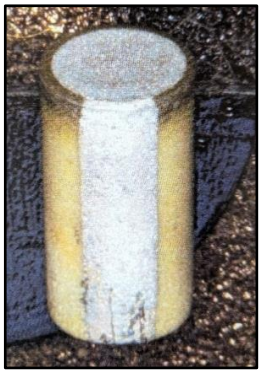

Figure 3. Commercial PZT Transducer

CHAPTER 3

EXPERIMENTAL PROCEDURES

According to Consortium X, the room temperature pulse-echo response of the transducers was measured using the standard pulse-echo method. The front of the transducers was immersed in water, then activated by a standard pulser, and the echo from a flat steel reflector was recorded using a digital oscilloscope. The measurement of the echoes was carried out with electrical matching circuitry connected to the transducer. Note, for illustrative purpose, all equipment used, instrument settings, and representative data are given in Figure 4. The frequency spectrum of a transducer's echo response was obtained using the fast Fourier transform (FFT) function of the oscilloscope, and all relevant frequency parameters and pulse echo sensitivity were determined. According to Consortium X, about 95% of the time the module passes the V_{PP} test, but the number of modules failing the original V_{PP} module test has increased over the last few years. To reiterate, the pulse echo sensitivity characterized by V_{PP} (net) < -26 dB is considered a failure.

Component:

- Acoustic Module

Equipment:

- Laptop: Acoustic Module Test
- Pulser/Receiver: JSR DPR300 (w/communications)
- Oscilloscope: LeCroy WaveJet 322A
- Fixture, Test, Pulse Echo, Module Test
- Fixture, Tank, Acrylic, Module Test

Materials:

- Water: DI & Degassed

Pulser/Reciever Setup

Switch/Knob	Setting/Position
Power	On
Receiver	Echo
Rel Gain (dB)	0 / 0 (tens / units)
HP Filter (MHz)	Out
LP Filter (MHz)	50
PRF Rate	10
Trigger	Int
Pulse Amplitude	16
Pulse Energy	Low 4
Damping	8

Oscilloscope Setup

Model Name	WJ322A
Time/div(second)	100n
Delay(second)	0
Delta(second)	0.000000001
Acquisition Mode	Normal
Trigger	Edge
Slope	Negative
CH1 Display	Off
CH2 Display	On
CH1 Volt/div	2V
CH2 Volt/div	100V
CH1 Offset	0V
CH2 Offset	192V
CH1 Coupling	DC1M
CH2 Coupling	DC1M
CH1 Bandwidth	Full
CH2 Bandwidth	Full

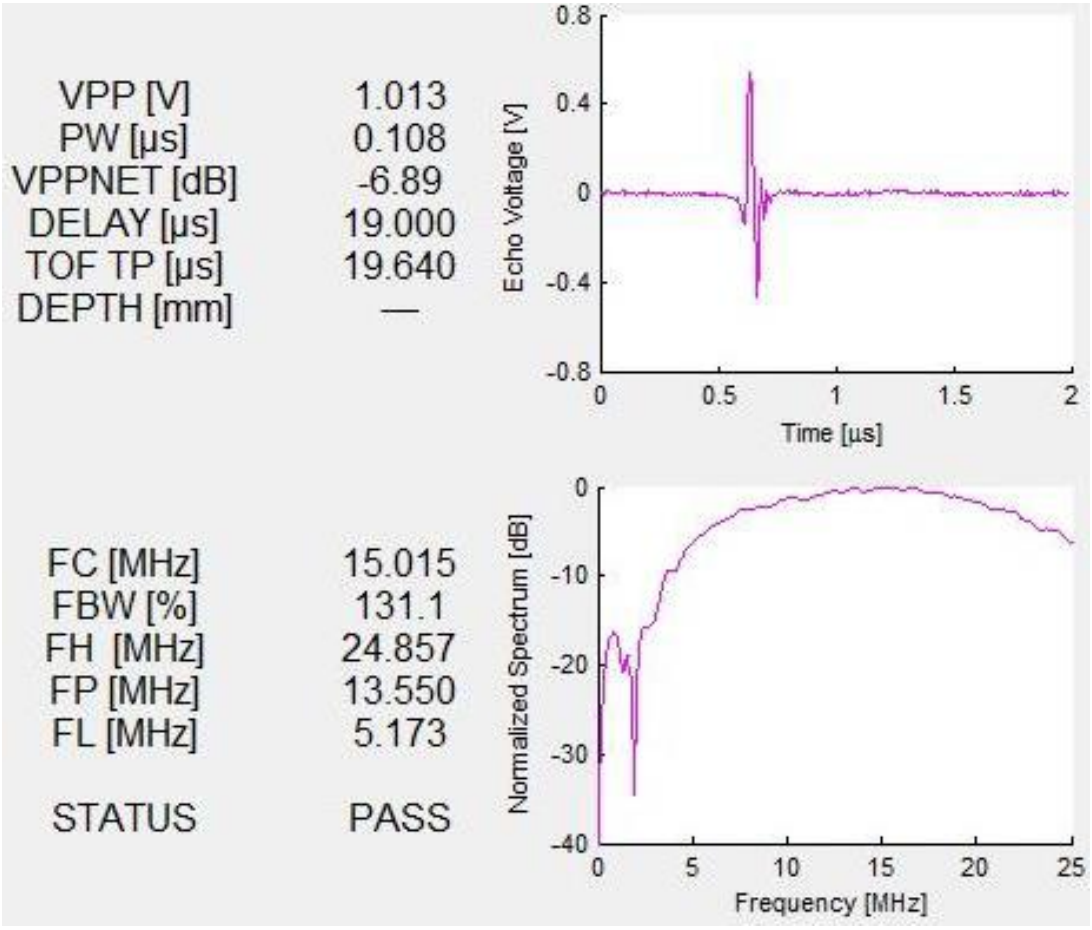

Figure 4: Equipment used, instrument settings, and representative data for the pulse-echo response of a passed module[2], [24].

To provide clues as to the origin(s) of failure, i.e., low pulse echo sensitivity, the objectives of the current work are to:

(A) Identify the individual layers of the multi-layered transducer stack; composition and thickness

(B) Determine the phase, microstructure, dopants and defects in the active pad PZT, and to ascertain their consistency in various samples

(C) Determine whether microstructural observations and alterations are manufacturing process induced or driving electrical field induced, and whether they can be related to the observed failure

The ceramic Pb $(Zr_{1-x}\,Ti_x)\,O_3$ (PZT) samples are to be thoroughly using a repertoire of advanced, physicochemical characterization techniques on both operational and failed samples. This analysis should uncover any identifiable characteristics that indicate raw material defects. The purpose of the emphasis on operational vs fail parts is to determine if operational parts begin to fail, post element manufacturing, due to assembly manufacturing or environmental variables that degrade PZT properties and/or introduce unknown failure modes. The central theme of the work is to identify potential inter-relationships between structure and properties of PZT. The overall motivation underlying this analysis is to increase the reliability during the lifecycle of the transducer by quantifying the causative factors and then incorporating remedial actions by predictive analysis and manufacturing test requirements, process changes, and/or drawing requirements.

The strategy of the analysis includes the spectrum of characterization methods listed in Table 1. The results of the preliminary analytical techniques (1-5 in Table 1) are used to determine if the PZT in the image element has the proper structure, phases, texture, and chemical composition. Significant variations in the manufacturing process can affect the piezoelectric properties, lower the Curie temperature, modify the piezoelectric aging rate, or allow for additional failure modes such as silver electromigration. In addition, tests are conducted to identify the presence of water, if any, within the PZT structure. The results of tests 1-5 directed tests 6 and 7 to delineate and quantify specific locations and failure modes within the PZT element.

Table 4. PZT Characterization Methods and Purposes

Method	Potential Results/Effects	Output-Purpose
1. Cu Kα XRD - X Ray Diffraction	Structure and Phases - Bulk/pad piezoelectric/nonpiezoelectric structures, phases, and textures that could lead to lower pulse echo or change aging characteristics post poling.	Phases (amorphous, lead deficient), Structure (perovskite), and Texture (preferred orientation of grains).
2. ICPE - PIXE - Inductively coupled plasma optical emission spectrometry and Proton-induced X-ray emission	Chemical Composition - Composition modifications, intended or unintended, that may affect aging, polarization, and/or shift Tc (Curie Temperature) characteristics via impurities, additives, and defects including isovalent dopants, and contaminants.	Chemical Composition - Determine the stoichiometry (Pb, Zr, and Ti, as well as potential isovalent dopants). Atomic percent (lower Tc and enhanced permivitty: Ba and Sr), and contaminants, shift curie temperature.

4. DGA / TGA - Differential gas analysis with Thermogravimetric c analysis	Endothermic or exothermic reactions recorded with increasing temperature to determine the presence of organic materials, incomplete sintered materials etc. in samples.	Differential gas analysis with thermogravimetric analysis to evaluate endothermic and exothermic reactions that occur with increasing temperature over time. Evaluation of DTA and TGA graphs.
5. HRTEM and FESEM - High resolution transmission electron microscopy and Field-emission scanning electron microscopy	Materials Structure - As warranted to complement and add definition to findings in XRD with respect to the atomic structure and issues such as Ag electromigration, grain size, lattice spacing, and structure (rhombohedral/tetragonal) that can dilute the electrical properties.	Crystal structure and microstructure in specific areas of the electrode/pad area and bulk PZT. Ag electrode migration-local areas, pyrochore, amorphous phases ratios/perovskite defects, cations second phases in grain boundaries/compensation mechanism. Ionic or electronic compensation. Complement and definition of findings in XRD with respect to the atomic structure and issues such as Ag electromigration, grain size, lattice spacing, and structure (rhombohedral/tetragonal).
6. TEM Transmission Electron Microscopy using HAADF.	Material Phases and Structure -Phase identification metrics, defects, and coupling coefficients requiring additional definition as defined in results of 1-5. Composition and diluents in material that modify electrical properties.	Phases/electron Diffraction/ structure/rhombohedral/unit cell/lattice spacing plus monoclinic phase
HAADF-High angle angular dark field imaging -Scatter based on atomic number	Material Mapping - Details on amorphous phases/Ag in pad area grain boundaries or other elemental maps as needed to quantify failure mode(s).	Elemental Maps-crystalline vs amorphous point by point map or Ag in pad area grain boundaries
7. XPS - X-Ray photoelectron spectroscopy	Electrical or Electrode degradation based on findings of 1-5. Titanium reduced dopant electronically affects tan losses. Figure of merit of transducer ability to transduce. Identify oxidation states of transition ions, and	Oxidation states of transition ions or possible dopant compensation mechanism.

	along with the results of 1-6 for possible dopant compensation mechanism. PZT characteristics or electrode interface.	

There are two broad categories of the characterization techniques used here: (a) average structure/phases/composition of homogenous/heterogeneous active PZT material (XRD, XPS; note that TGA/DTA gives additional information such as weight losses and thermal events during heating) and (b) local structure and inhomogeneities such as defects, precipitates, interfaces, phases/chemistry at the atomic level (HRTEM, STEM, EELS, HAADF). Note, specific regions of the active PZT requires arduous sample preparation procedures, systematic test sequences, and analyses reported here. The sample identification was as follows; partial or fully complete transducer stacks (module) obtained from Consortium X:

1) Operational: Samples which have passed E-field tests.
2) Fail: Samples which have failed E-field tests.
3) Pad: Active PZT layer in transducer.
4) Substrate: PZT layer which is used as backing layer.
5) Parylene: A polymer coating for protection.
6) Uncoated: Samples without Parylene (polymer) coating and not subjected to E-fields.
7) Coated: Samples with Parylene (polymer) coating and not subjected to E-fields.

3.1 X-ray Diffraction (XRD):

Instrument model is Bruker D8. A versatile, non-destructive analytical technique for identification and quantitative determination of the structures and various crystalline forms, known as ‘phases’, of compounds present in powdered and solid samples. Identification is achieved by comparing an XRD pattern obtained from an unknown sample with an internationally-recognized database. Instrument X-rays are Cu Kα of wavelength (λ) = 1.541 Å, 2θ scan range: 20-70º. A Beam Collimator is used to reduce X-ray beam diameter to, 1 mm; focused on center of sample surface (Figure 1). Sample mounted on clay and petroleum jelly to eliminate X-ray interference with surfaces other than sample surface. Each sample is exposed to X-rays for an average of 365 scans[26].

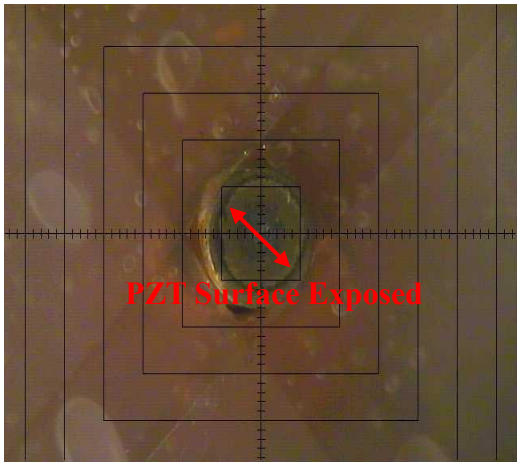

Figure 5. Sample surface exposed of X-rays.

3.1.1 XRD Samples Preparation:

To remove layers, polishing was performed on a “variable speed polisher and grinder” instrument (Ecomet) at 90 rpm, using glycol-based polycrystalline (3 µm) diamond suspension and high viscosity propylene glycol-based Red Lube lubricant on a

polishing cloth. The top surfaces of PZT were concave, with vertical height (from bottom center and top edge of bowl) between 25-50 μm for all samples. Samples were initially polished to level off the top surface and then the Parylene and Ag layers were removed to expose the PZT pad. With the help of a microscope, which can determine focus-dependent depth measurement at 400X magnification, controlled polishing and measurement of the thickness of layers removed were carried out with a precision ±5 μm.

3.2 Differential Thermal Analysis (DTA)/(Thermogravimetric Analysis (TGA)[27]:

Instrument model is LABSYS EVO DTA/TGA. TGA determines decomposition/mass loss over a temperature range. DTA determines endo- and exothermic event temperatures.

3.3 Inductively Coupled Plasma -Mass Spectrometry Laser Ablation (ICP-MS LA) [28]:

Instrument model is ELAN 6000 quadrupole ICP-MS. This technique is used for in-situ analyses of trace elements and for mapping spatial variation of elemental composition within the sample. The principle of this technique is that a high energy ultra-violet laser produces craters in the sample ranging in size from 2 microns to 12 microns, depending on the requirement. The material is ablated and moved from the sample into the plasma of ICP-MS and the material is then ionized. The LA system is fully computer controlled with a real-time video imaging system capable of reflected and transmitted light (polarized light available) viewing. This technique can determine many trace elements down to low ppm or even ppb levels, although absolute detection levels are highly element, sample matrix and spot size dependent [15].

For ICP-MS LA, the sample must be of matrix for which a calibration standard reference material (SRM) of close matrix match is available. For PZT ceramics, there are

no SRM standards available anywhere and hence this analysis acts as a complementary to EPMA-WDS.

3.4 Electron Probe Microanalyzer (EPMA)- Wavelength Dispersive X-ray Spectrometer (WDS):

Instrument model is CAMECA SX50. WDS, equipped with five different spectrometers, is used to perform quantitative analysis. This technique provides very high and accurate quantitative chemical analyses data. The analysis can be carried out on small solid samples (>1 mm) and is a non-destructive technique. WDS spectrometers scan over a predetermined wavelength range and the intensity of the x-rays detected are plotted versus wavelength (or energy), and elements present are identified by peak matching. A reasonable full scan for all elements from Boron to Uranium can be obtained. WDS analysis can determine the presence of trace elements (< 0.1 wt%) in an unknown sample and identify suitable background positions and potential interferences. The resolution of the results can be improved by using longer dwell time, multiple scans and high energy electron beams. The technique demands very high sample surface quality, which involves polishing the surface to <0.05 microns surface roughness [29].

3.4.1 Electron Probe Microanalyzer (EPMA)- Wavelength Dispersive X-ray Spectrometer (WDS) Sample Preparation

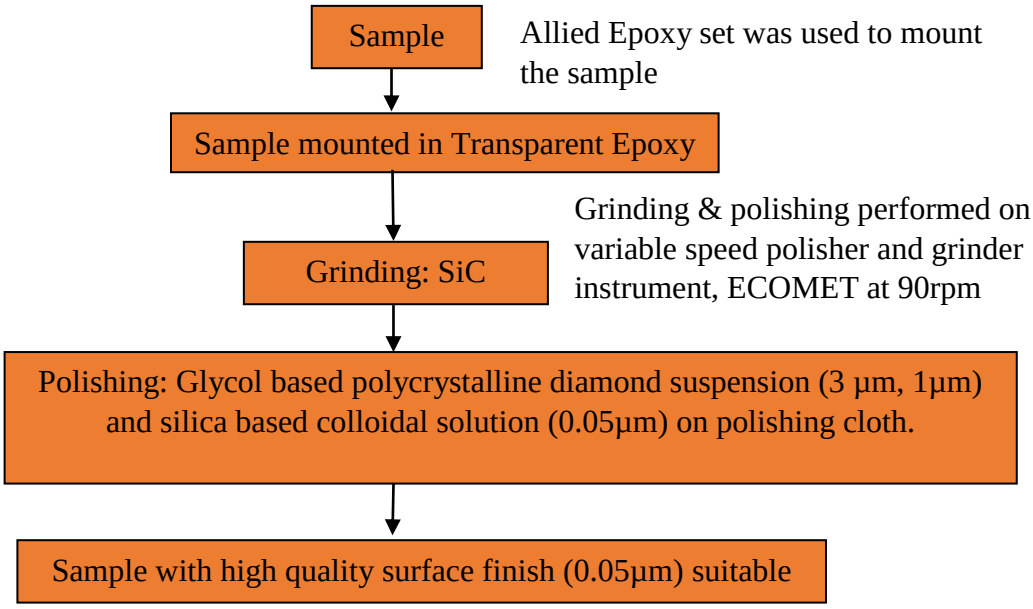

3.5 X-ray Photoelectron Spectroscopy (XPS):

Instrument model is Kratos 165 Ultra Photoelectron Spectrometer. This technique is used to extract elemental composition and chemical bonding information (valence states of elements) on the sample's surface. XPS is also referred to as Electron Spectroscopy for Chemical Analysis.

XPS provides the energy resolution needed to detect elemental peak position, and energy shifts due to chemical bond formation. Information is typically obtained for the region within 4-5 nm of the outer surface. Angle resolved XPS can allow analysis of regions even closer to the sample surface. Relative atomic concentration percentages can be determined with a sensitivity of 0.1 to 1 atomic % for Li and heavier elements. Analysis is carried out in an ultrahigh vacuum (~10^{-9} Torr or better) system [30].

3.6 Electron Probe Microanalyzer (EPMA)- Energy Dispersive X-ray Spectrometer (EDS):

Instrument model is JXA-8530F Electron Probe Microanalyzer (EPMA). EDS is used for the identification of constituent elements in a specimen and the study of their distribution. Analyses are performed by illuminating the specimen surface with a finely focused electron beam and measuring the wavelengths and intensities of characteristic X-rays emitted from the specimen. It is integrated with a silicon-drift detector (SDD) energy dispersive X-ray spectrometer (EDS)). The Schottky field-emission electron gun (FEG) and the optical system provide small probe diameter even at low acceleration and large current. The observation screen allows you to observe a high-definition scanning image in real time with 1280x960 pixels, save a scanning image up to 5120x3840. For combinations of elements, however, the EDS system is less desirable than WDS because of its limited spectral resolution (overlapping peaks) and limited sensitivity. However, EDS is used to quickly determine what elements are present in a sample[31].

3.7 Scanning Transmission Electron Microscopy (STEM):

The ARM200F is an aberration-corrected scanning transmission electron microscope (STEM) equipped with both an x-ray spectrometer, and a newly developed electron spectrometer (ultra-fast EELS) that allows atomic level mapping. The ARM200F offers resolution of 0.8 Å at 200 kV. The Schottky field emission gun and a CEOS CESCOR hexapole aberration corrector enables imaging resolution of 78 picometers at beam current densities of 8 nA/nm^2. The JEOL 50 mm^2 (0.3 St.) windowless light-element-sensitive X-ray detector and a Gatan Enfinium EELS (Electron Energy Loss) spectrometer are used for high spatial resolution and high sensitivity microanalysis[32], [33].

The microscope can be operated in high angle and medium angle annular dark-field STEM modes as well as bright field and annular bright field modes.

High Resolution Transmission Electron Microscopy (HRTEM):

The CM200 HRTEM can provide structural information at better than 0.2 nm spatial resolution. When recorded under optimum conditions, electron micrographs can be directly interpreted in terms of the projected crystal potential. Specimen Requirements: For highest resolution, specimens must be <40 nm thick. Energy Dispersive X-ray Microanalysis (EDX) is a microanalytical technique that uses the characteristic spectrum of x-rays emitted by the specimen after excitation by high-energy electrons to obtain information about its elemental composition. The ranges of elements detectable by EDX and electron energy loss spectroscopy (EELS) are somewhat complementary; EDX is generally better suited to detecting elements of high atomic number (Z), whereas EELS can readily detect low-Z elements. Unlike EELS, EDX does not provide quantitative information (except through quantitative chemical analysis in some cases). Compared to EELS, EDX is a relatively simple technique and provides rapid qualitative microanalysis of the specimen[32], [33].

3.7.1 STEM/TEM Sample Preparation: Focused Ion Beam (FIB)

FEI Nova 200 Dual-Beam FIB comes with the combined ultra-high-resolution field emission scanning electron microscopy (SEM) and precise focused ion beam (FIB) capabilities. This instrument is used to prepare samples with thickness as low as 50 nanometers for TEM analysis. Each sample preparation takes at least 3 hours. In the FIB sample preparation after selecting the area to investigate, a micron thick strip of Platinum is electro-deposited to protect the area-of-interest beneath from being contaminated by Ga

ions. The electron beam is maintained at 5 kV and a current of 6.3 nA. The selection is made to mill away the specimen on both sides of the Platinum strip using the Gallium ion beam, maintained at 30 kV and 7 nA. The milled specimen is attached to a graphite electrode and lifted out after cutting from the parent sample. The lifted specimen is attached to a molybdenum grid and is milled to nano-scale thickness, first at 100 pA and then at 10 pA ion beam currents to final thickness of <50 nm[34].

3.7.2 Manual STEM/TEM Sample Preparation:

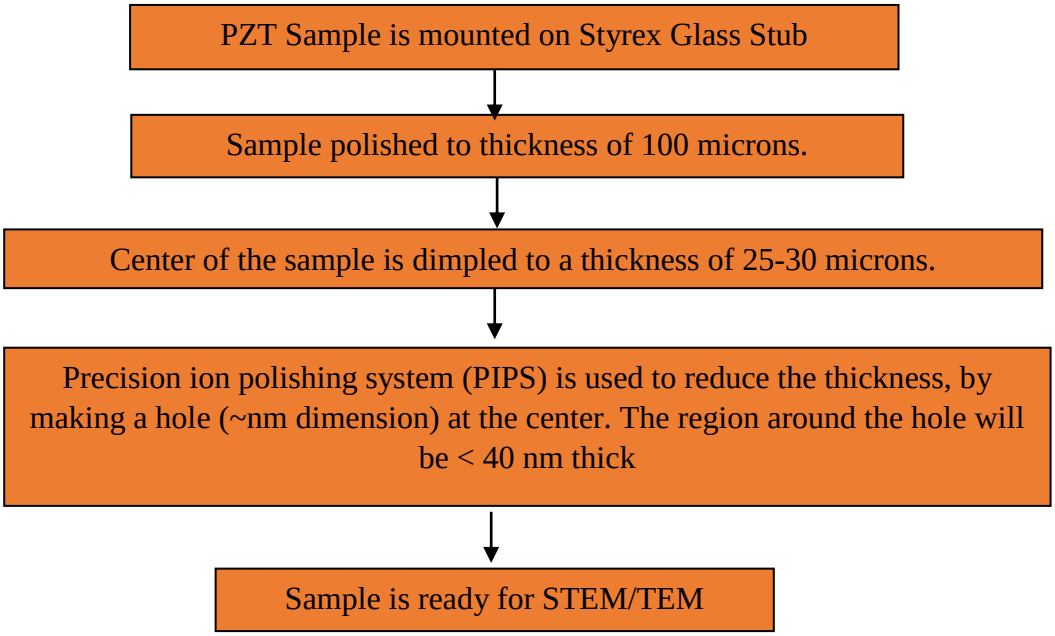

CHAPTER 4

RESULTS AND DISCUSSION

4.1 X-ray Diffraction (XRD) and DTA/TGA:

The following Figures 5-30 shows XRD and DTA/TGA data for different samples. The identification for each sample is given in Table 5. Each sample is analyzed by XRD first, then evaluated with DTA/TGA, and the post DTA/TGA sample is again subjected to XRD. The operational samples, mentioned in Table 5, have passed the electrical tests by exhibiting good pulse echo sensitivity when subjected to electrical tests and the ones with fail did not pass the tests. All Pad PZT samples exhibit both tetragonal and rhombohedral peaks indicative of the MPB composition. All substrate PZT samples exhibit 100% tetragonal peaks. The c/a ratio for all the samples is almost same and concur with reported literature values for PZT (52/48)[35]. This indicates that the composition of all samples is $PbZr_{0.52}Ti_{0.48}O_3$. The ratio of intensities of tetragonal (200), (002) and rhombohedral (200) peaks in the 2θ 43-45º is calculated in the Table 5. The pad PZT samples did not exhibit a specific trend. The fraction of intensity of tetragonal peaks varies in all Pad PZT samples. This variations of the Zr to Ti ratio within a sample and between samples is an indicative of a lack of process reproducibility. For all pad PZT samples, intensity of tetragonal peaks before and after DTA are different. This shows that further reactions (which also remain incomplete due to persistence of DTA peaks) occur at much lower temperatures after sintering, and those reactions remain incomplete after calcination and sintering.

Table 5. XRD Results

Sample	c/a Ratio	% $(I_{200T}+I_{002T})/(I_{200T}+I_{002T}+I_{200R})$
1. Operational 1-Pad: Before DTA	1.022	41
2. Fail 1-Pad: Before DTA	1.022	63.4
3. Operational 2-Pad: Before DTA	1.021	84
4. Fail 2-Pad: Before DTA	1.024	54.4
5. Uncoated 1-Pad: Before DTA	1.023	43.6
6. Operational 1-Substrate: Before DTA	1.022	100
7. Fail 1-Substrate: Before DTA	1.023	
8. Operational 2Substrate: Before DTA	1.022	
9. Fail 2-Substrate: Before DTA	1.023	
10. Uncoated 1-Substrate: Before DTA	1.022	
1. Operational 1-Pad: After DTA	1.026	77.4
2. Fail 1-Pad: After DTA	1.022	52
3. Operational 2-Pad: After DTA	1.009	72
4. Fail 2-Pad: After DTA	1.012	73
6. Operational 1-Substrate: After DTA	1.021	100
7. Fail 1-Substrate: After DTA	1.021	
8. Operational 2-Substrate: After DTA	1.022	
9. Fail 2-Substrate: After DTA	1.021	

Table 6 shows the exothermic peaks noted at different temperatures in the analyzed samples. An ideal PZT material should not show any peaks after 270 degrees Celsius, given that sintering procedure is supposedly completed at much higher temperatures. The

samples analyzed for DTA/TGA are identified in Table 6. All the samples have peaks 1, 2 & 3 at similar range of temperatures. The presence of exothermic peaks at higher temperatures shows that the material is incompletely calcined. Repeated DTA/TGA runs still shows similar exothermic peaks indicating that the presence of incompletely calcined material is predominant.

Table 6. DTA/TGA Recorded Peaks

Sample ID	Peak 1 (ºC)	Peak 2 (ºC)	Peak 3 (ºC)
1. Operational 1-Pad	400	480	525
2. Fail 1-Pad	400	475	525
3. Operational 2-Pad	385	475	500 & 521
4. Fail 2-Pad	375	425	525
5. Operational-1 Substrate	375	470	495
6. Fail 1-Substrate	375	470	485
7. Operational 2-Substrate	-	470	535
8. Fail 2-Substrate	391	475	537
9. Uncoated 1-Pad	375	475	550
10. Operational 2-Pad (Second DTA Run)	355	455	489
11. Fail 2-Pad (Second DTA Run)	370	465	485

Figure 6 is the diffraction pattern of sample 1 operational pad, which shows the presence of tetragonal $(002)_T$, $(200)_T$ and rhombohedral $(200)_R$ peaks and indicative of the MPB composition. The DTA/TGA data for sample 1 (Figure 7) shows exothermic peaks

at three different temperatures (Table 6) with negligible weight loss. This indicates presence of un-calcined material in the pad. The XRD data of sample 1 after DTA/TGA (Figure 8) shows the similar tetragonal and rhombohedral peaks, but the relative intensities of tetragonal and rhombohedral peaks are very different from that obtained prior to DTA/TGA. The $(002)_T$ peak dominates in the post DTA/TGA diffraction pattern whereas $(200)_R$ dominates before TGA. The presence of un-calcined material means parts of pad layer is not piezoelectric, which does not contribute to the electromechanical properties, and therefore, to pulse echo signal. To achieve the desired properties, the transducer will have to be subjected to very high E-fields.

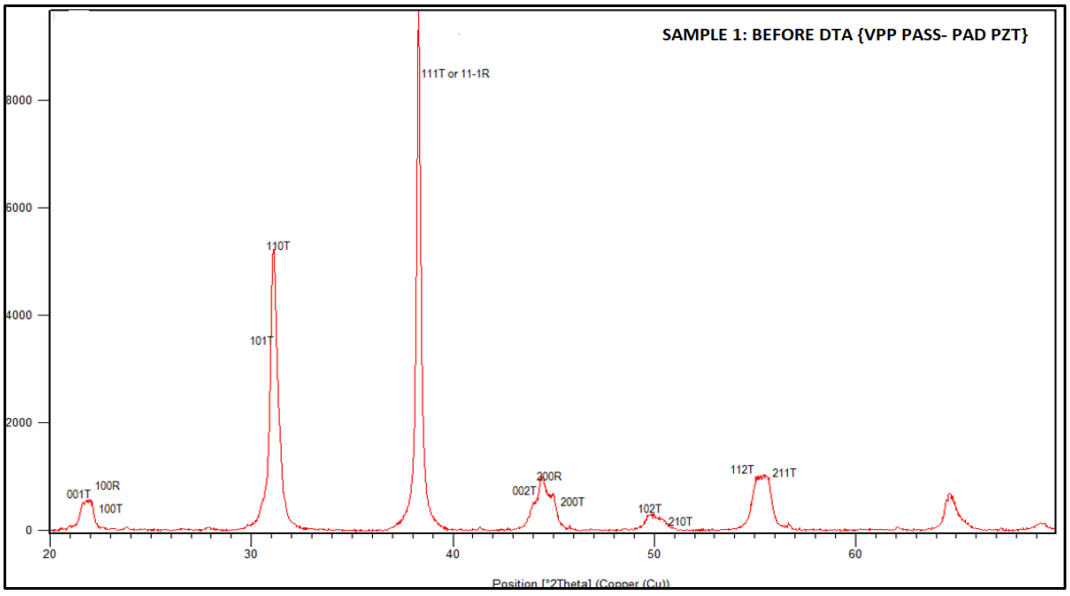

Figure 6. Sample 1, before TGA/DTA analysis.

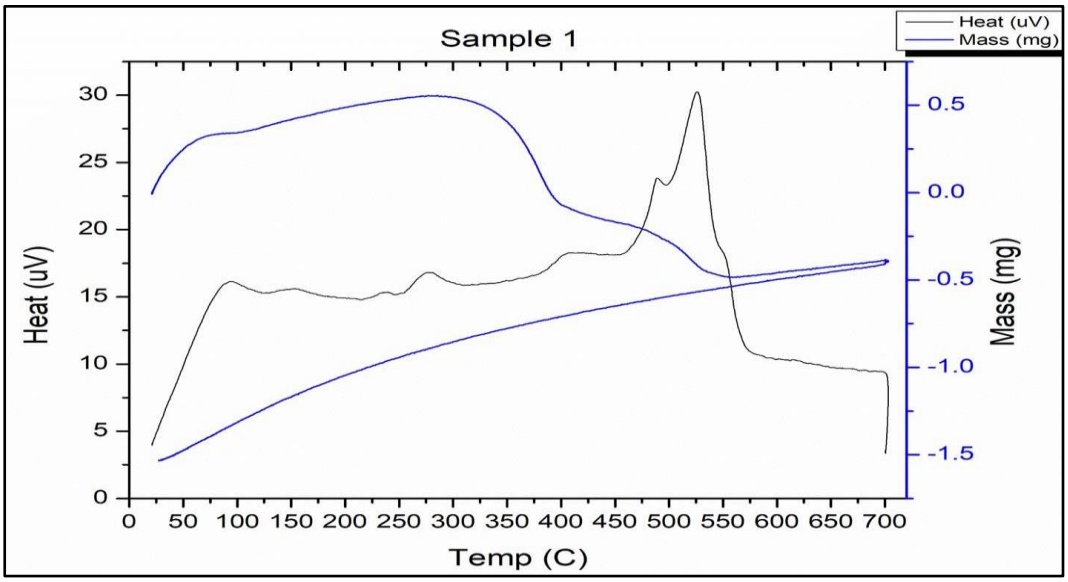

Figure 7. Sample 1 DTA/TGA graph.

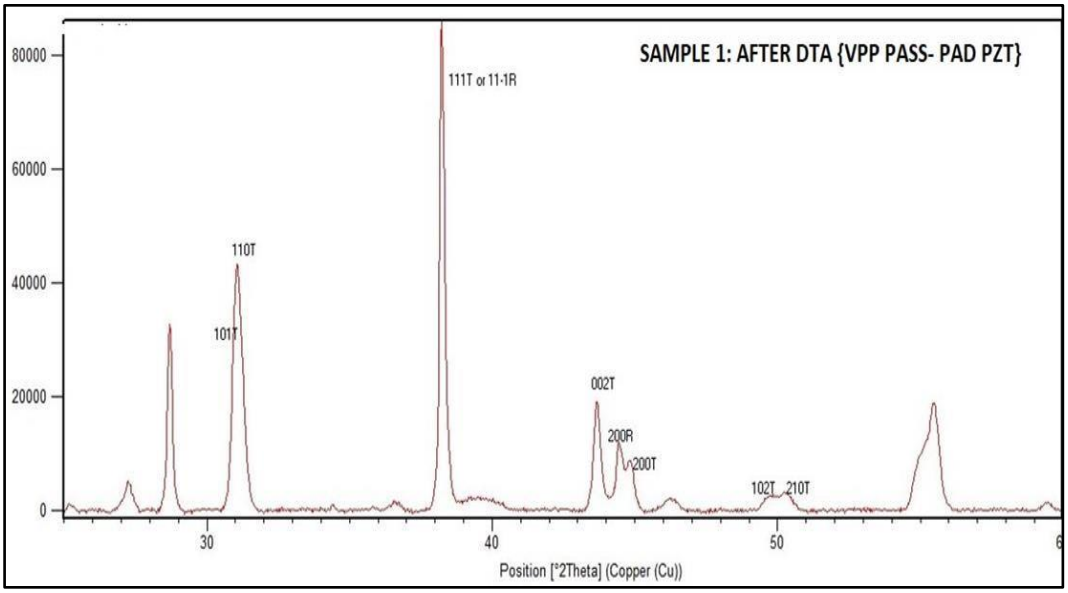

Figure 8. Sample 1, after TGA/DTA analysis.

Figure 9 is the diffraction pattern of sample 2 fail pad, which shows the presence of tetragonal $(002)_T$, $(200)_T$ and rhombohedral $(200)_R$ peaks and indicative of the MPB composition. The DTA/TGA data for sample 2 (Figure 10) shows exothermic peaks at

three different temperatures (Table 6) with negligible weight loss. The XRD data of sample 2 after DTA/TGA (Figure 11) shows similar tetragonal and rhombohedral peaks, but the relative intensities of tetragonal and rhombohedral peaks are very different from that obtained prior to DTA/TGA. The $(200)_R$ peak dominates in both the diffraction patterns.

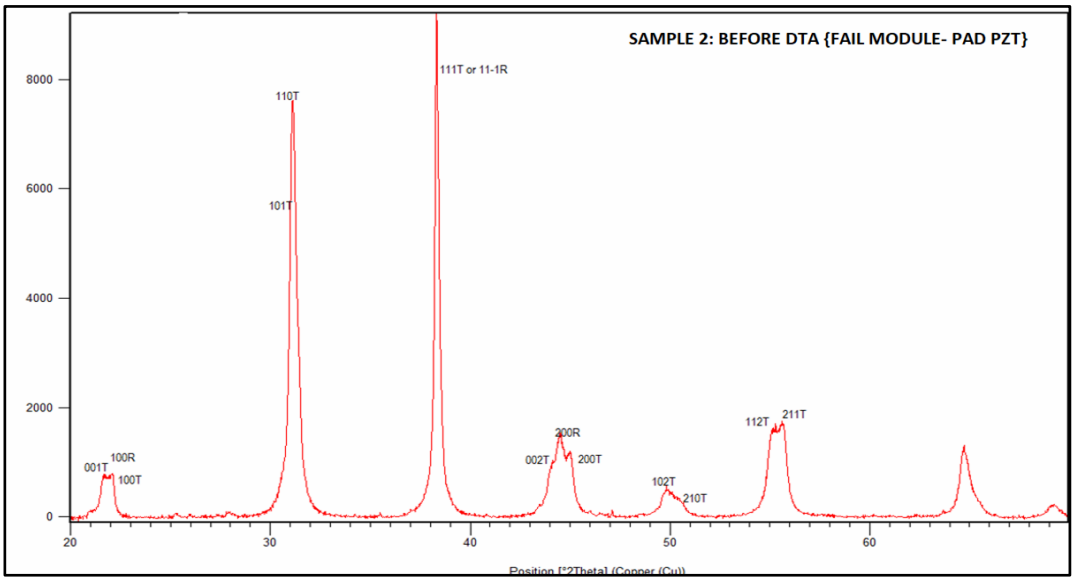

Figure 9. Sample 2, before TGA/DTA analysis.

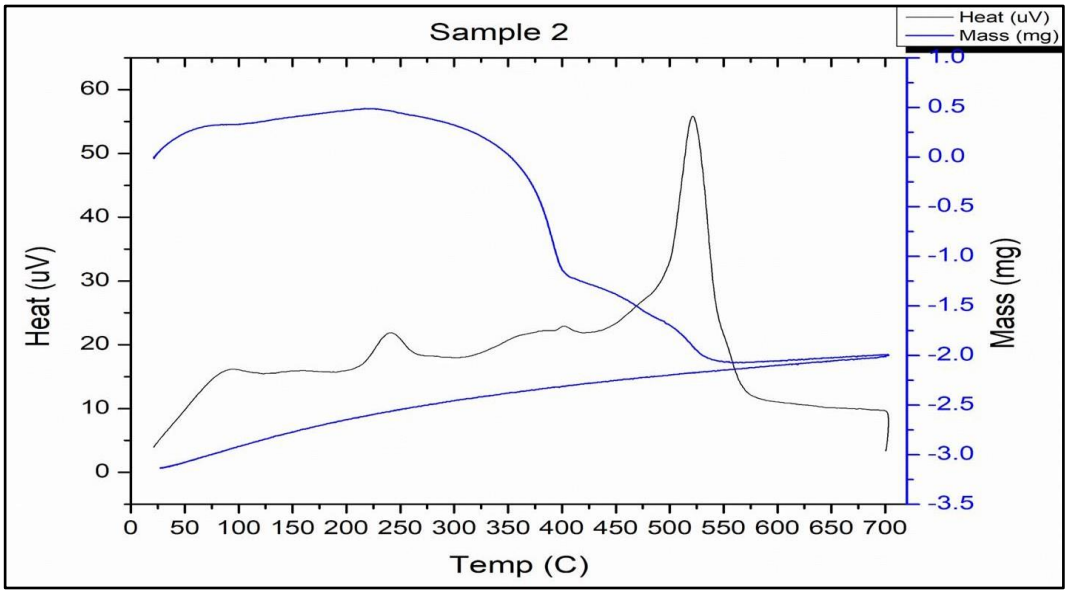

Figure 10. Sample 2 DTA/TGA graph.

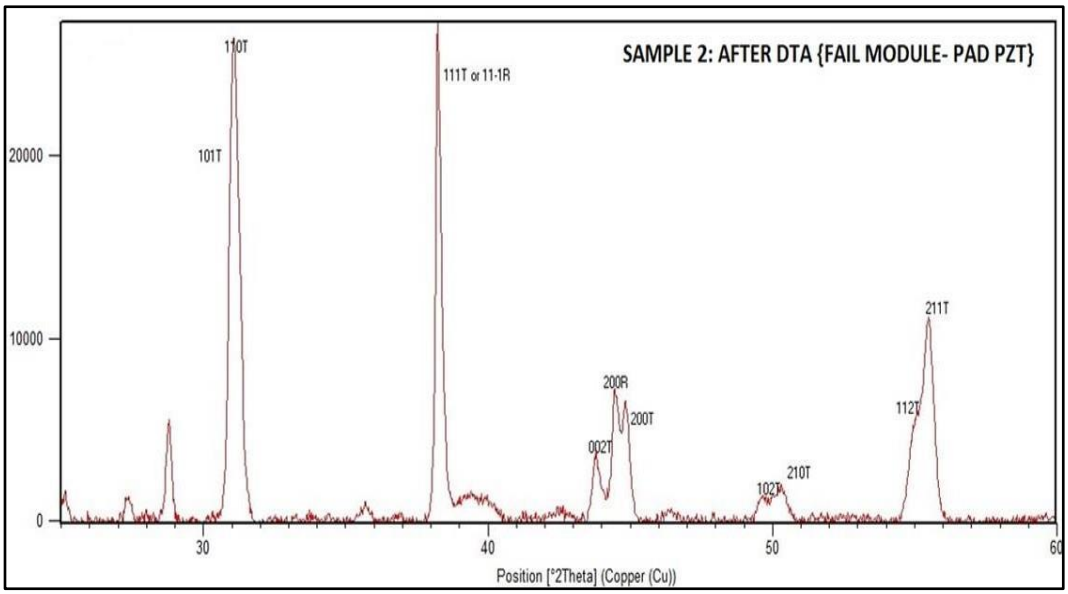

Figure 11. Sample 2, after TGA/DTA analysis.

Figure 12 is the diffraction pattern for uncoated sample which shows presence of tetragonal $(002)_T$, $(200)_T$ and rhombohedral $(200)_R$ peaks and indicative of the MPB composition. The $(200)_R$ peak dominates in this pattern.

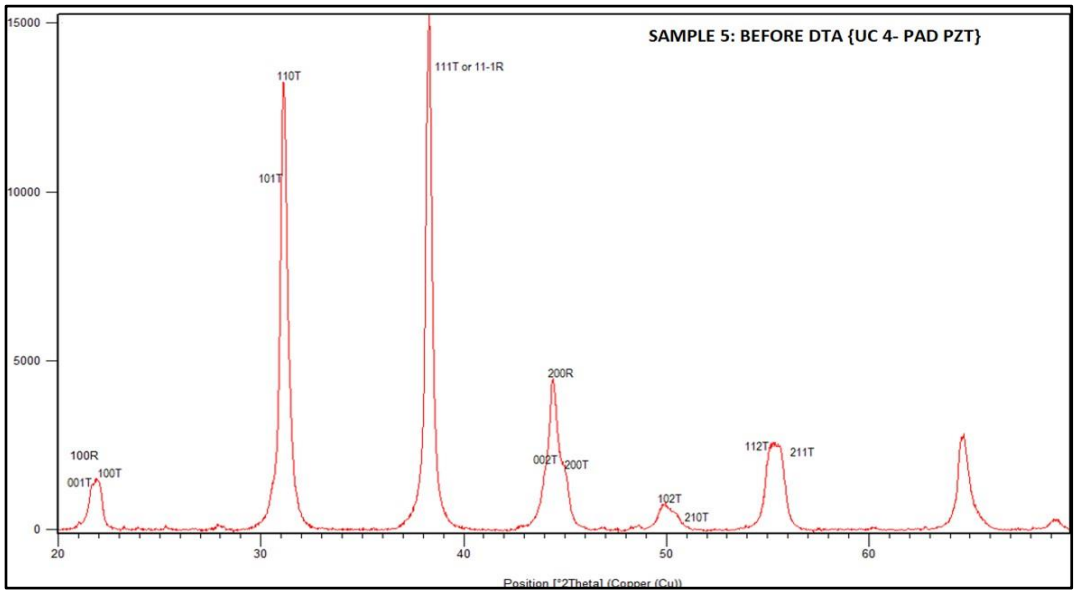

Figure 12. Sample 5, before TGA/DTA analysis.

Figure 13 is the diffraction pattern of sample 6 operational substrate, which shows the presence of tetragonal $(002)_T$ and $(200)_T$ peaks. No rhombohedral $(200)_R$ peak is observed. The DTA/TGA data for sample 6 (Figure 14) shows exothermic peaks at three different temperatures (Table 6) with negligible weight loss. The XRD analysis of sample 6 after DTA/TGA (Figure 15) shows similar tetragonal peaks.

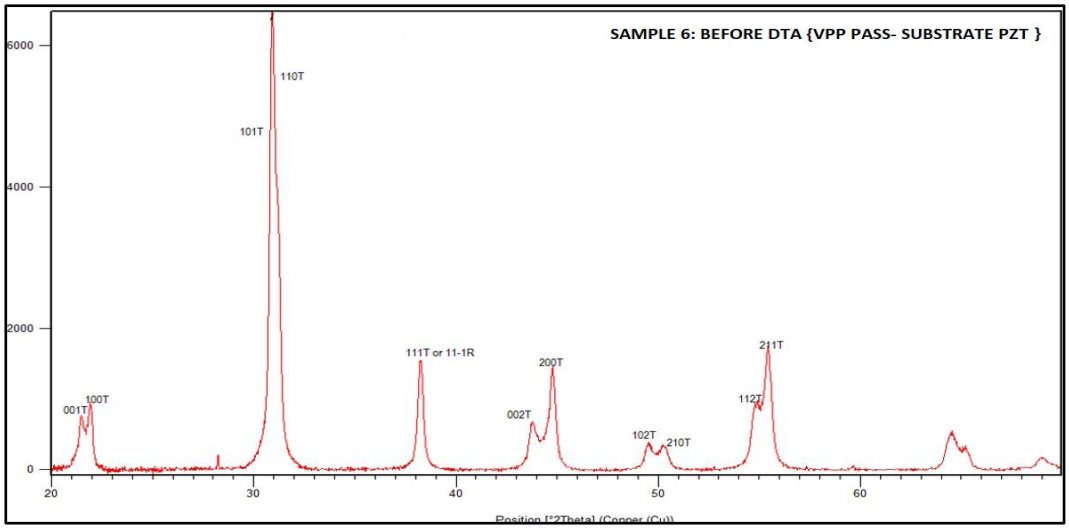

Figure 13. Sample 6, before TGA/DTA analysis.

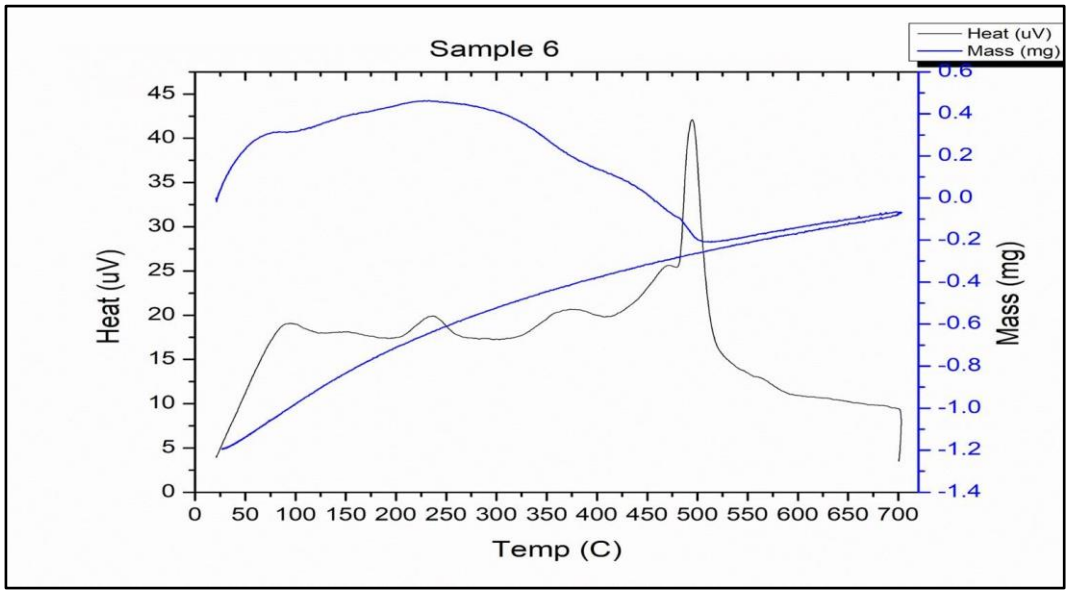

Figure 14. Sample 6 DTA/TGA graph.

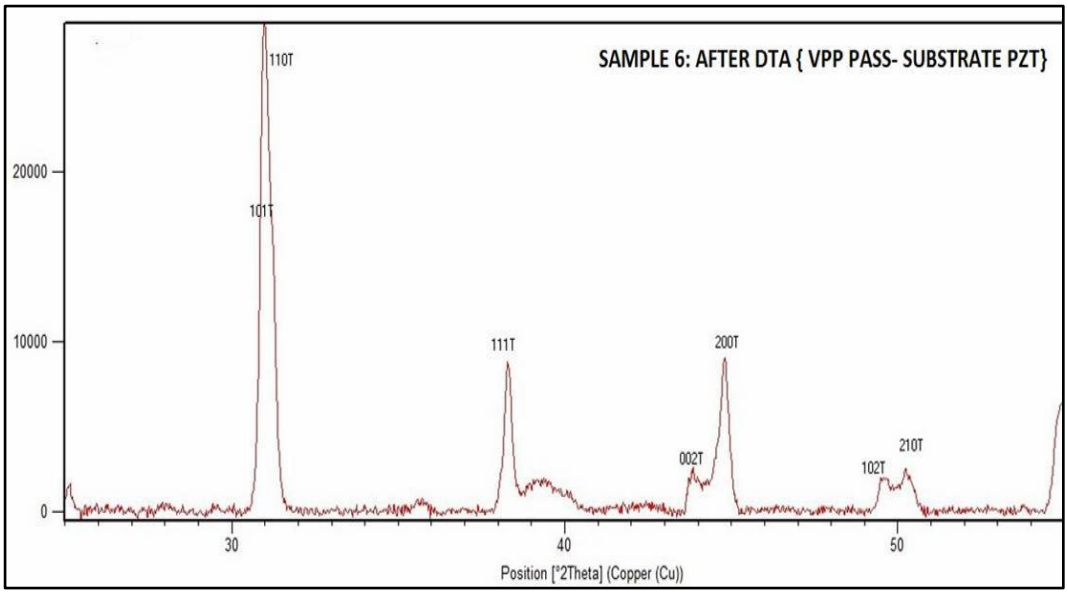

Figure 15. Sample 6, after TGA/DTA analysis.

Figure 16 shows the diffraction pattern of sample 9 fail substrate, which shows the presence of tetragonal $(002)_T$ and $(200)_T$ peaks. No rhombohedral $(200)_R$ peak is observed. The DTA/TGA data for sample 7 (figure 17) shows exothermic peaks three different temperatures (table 6) with negligible weight loss. XRD analysis of sample 9 after DTA/TGA (figure 18) shows the similar tetragonal peaks.

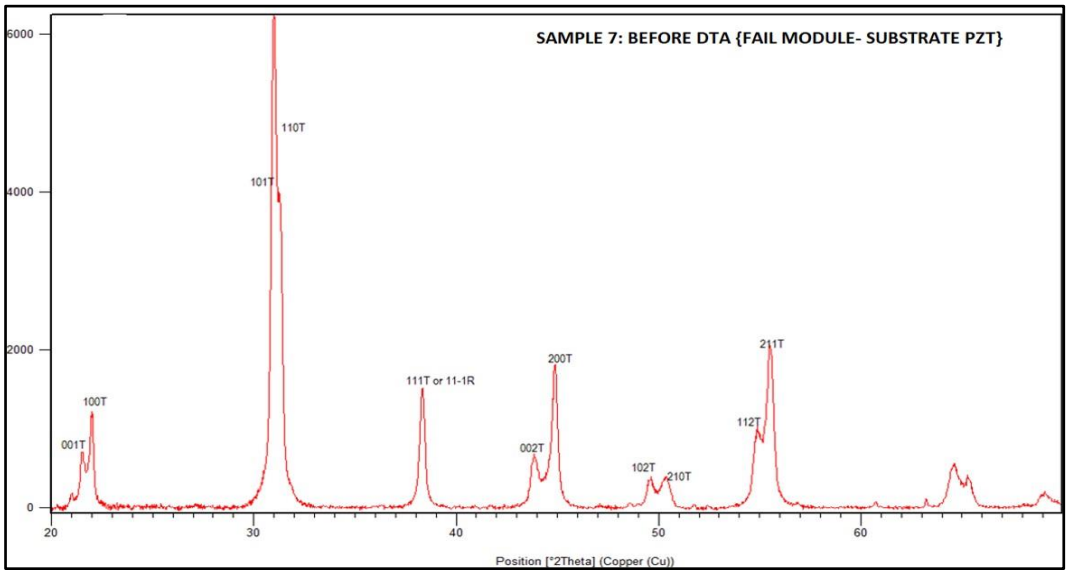

Figure 16. Sample 7, before TGA/DTA analysis.

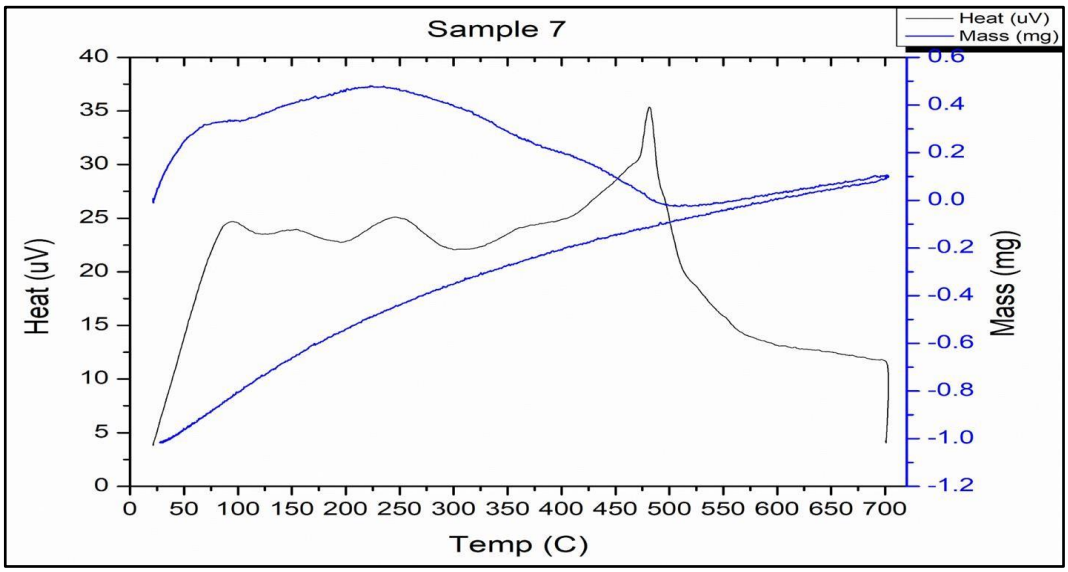

Figure 17. Sample 7 DTA/TGA graph.

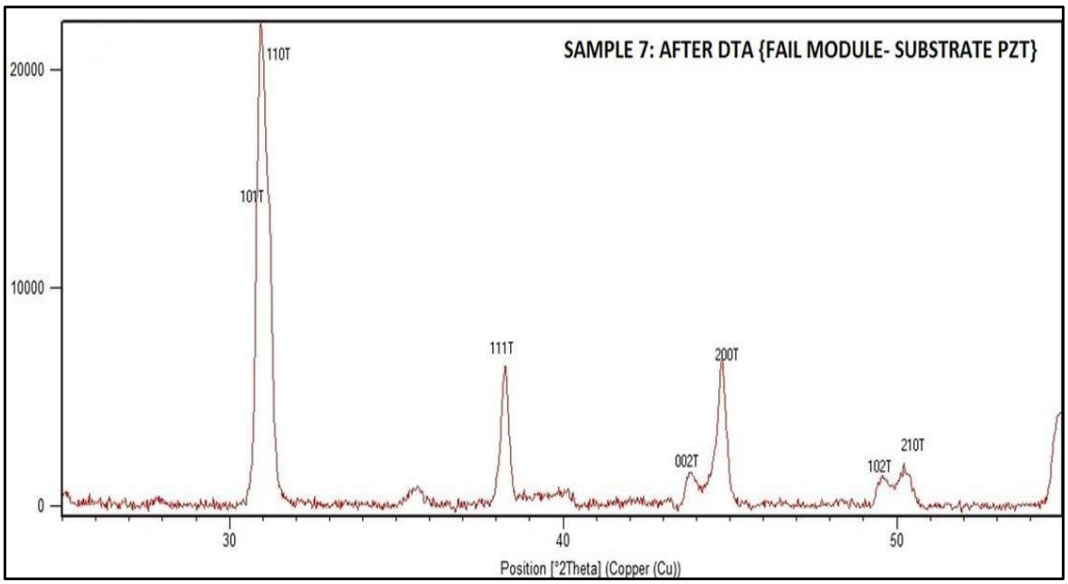

Figure 18. Sample 7, after TGA/DTA analysis.

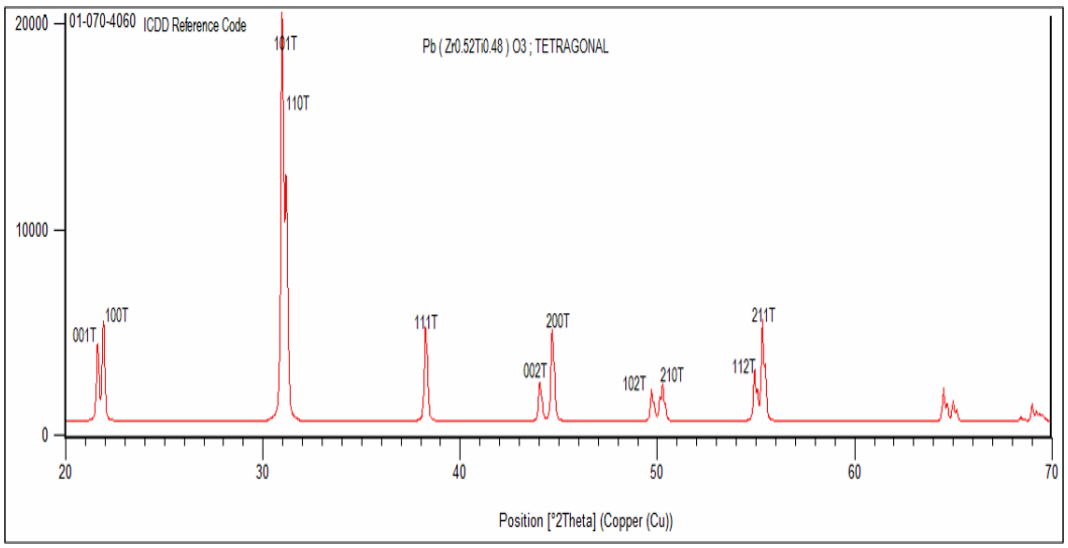

Figure 19. PZT ICDD 01-070-4060.

Figure 19 shows the PZT (52/48) ICDD standard graph. The identification of the samples is give in Table 3.

4.2 ICP-MS Laser Ablation:

The ICP laser ablation results are used as complementary to EPMA-WDS. Since there are no material standards available for PZT, the results are not quantitative.

The operational and fail pad samples shows presence of elements Mn, Cu, Sb, Si and Al. The elements Mn, Sb and Al are hard dopants whereas presence of Si is due to polishing contamination. The presence of Cu is perhaps from the Pb-based sintering aid to reduce the sintering temperatures. Whereas the operational and fail substrate samples shows no dopant presence.

Table 7. ICP-MS Laser Ablation Results

Sample ID	Elements Detected	Remarks
Operational-1 Pad PZT	P, Mn, Cu, Y, Nb, Sb, Al, Si.	Y & Nb detection is due to overlapping of peaks with other elements and hence not considered as constituent elements.
Failed- Pad PZT	P, Mn, Cu, Y, Nb, Sb, Al, Si.	
Operational-1 Substrate PZT	Y, Nb,	
Failed- Substrate PZT	Y, Nb,	

4.3 EPMA-WDS:

From Table 8 below, the back calculated formula shows dopants and excess PbO. The calculation of formula shows that the material is PZT with Zr/Ti ratio as 52/48; Pb $(Zr_{0.52}\ Ti_{0.48})\ O_3$. The dopants identified are Sb, Mn, Al, and Cu. Also, excess PbO content

is observed in fail pad samples compared with operational pad samples, but negligible excess PbO content is observed in all substrate samples. The WDS results are supported by ICP-MS laser ablation analysis.

Table 8. WDS Results

Sample ID	Excess PbO (wt %)	Total Dopants (Sb, Mn, Al, Cu) at %	PZT (52/48) with moles of excess PbO
Operational 1-Pad	12.49	1.2	(PZT). 0.219 PbO
Fail 1-Pad	6.25	1.6309	(PZT). 0.0993 PbO
Operational 2-Pad	15.41	1.0859	(PZT). 0.279 PbO
Fail 2-Pad	6.47	1.4848	(PZT). 0.106 PbO
Operational 1-Substrate	2.01	0.374	(PZT). 0.03 PbO
Fail 1-Substrate	1.34	0.3673	(PZT). 0.0198 PbO
Operational 2-Substrate	1.34	0.3564	(PZT). 0.0199 PbO
Fail 2-Substrate	1.34	0.3489	(PZT). 0.0166 PbO

4.4 XPS:

Survey scan shows the presence of Pb, O, C, Ti, and Ag. Zr after scanning the Zr 3d region at~182 eV binding energy. The concentration of Cu was too low on the surface to be detected by XPS. Note, Mn, which is in very low concentration, is difficult to detect in samples containing Pb. The Mn 2p has the highest sensitivity for Mn but it overlaps with Pb $4p_{3/2}$ peak. The Mn 3s peak, which would be useful to determine its oxidation state, overlaps with Pb 5p peak, and the Sb 3d peak overlaps with O 1s peak. The Sb 3p peak has lower sensitivity but even with 1.8 s of integration time, it could not be detected due to its low concentration. Although Ag was found on the surface, Al was not detectable due to its

low concentration. The low concentrations of Mn, Sb, Al, and Cu are below the detection limits (0.5-1 atomic %) of XPS.

Table 9. XPS Results

Sample ID	Elements Detected
Operational-1 Pad	Pb, C, O, Ti, Ag, Zr
Failed-2 Pad	
Operational-1 Substrate PZT	

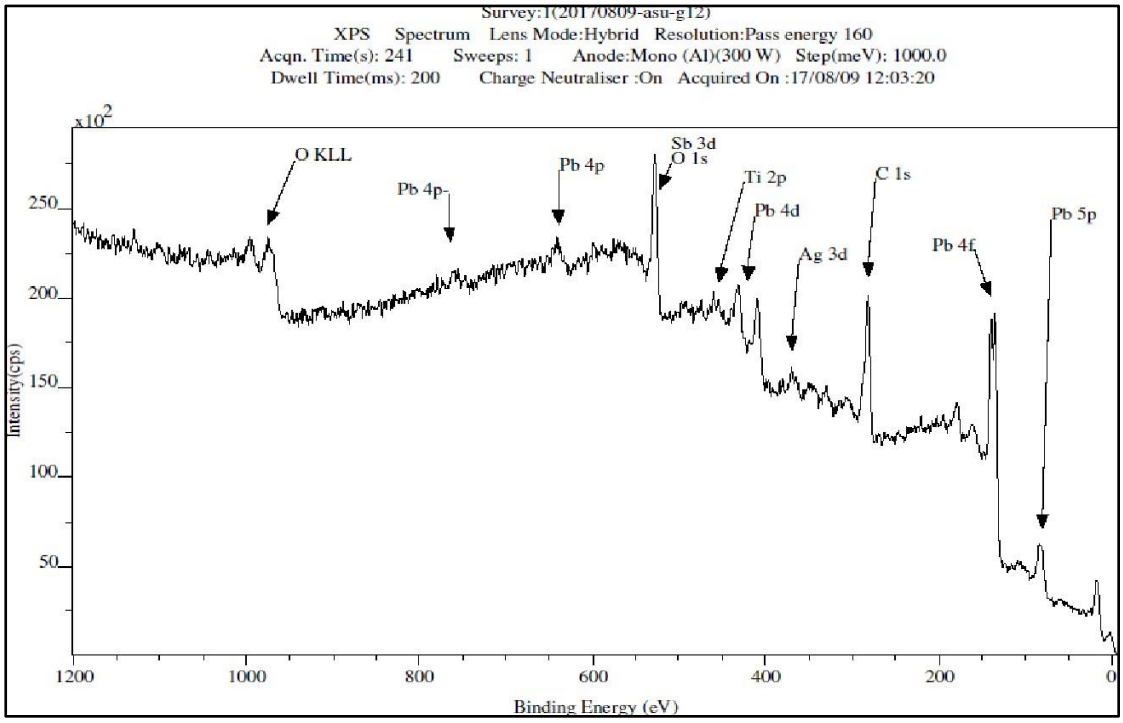

Figure 20. XPS spectrum of operational-1 pad.

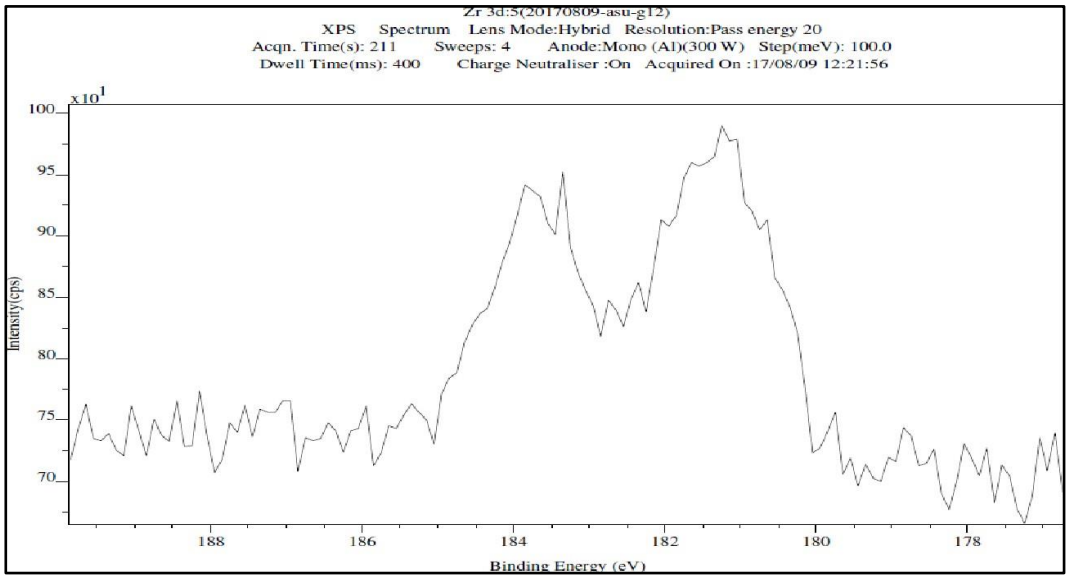

Figure 21. XPS Zr 3d lines, operational-1 pad.

4.5 Optical Microscopy and SEM:

Figure 22 shows the optical micrograph of uncoated sample; sample not coated with Parylene and not subjected to poling. Noted severe discontinuities in the Au and Ag layers.

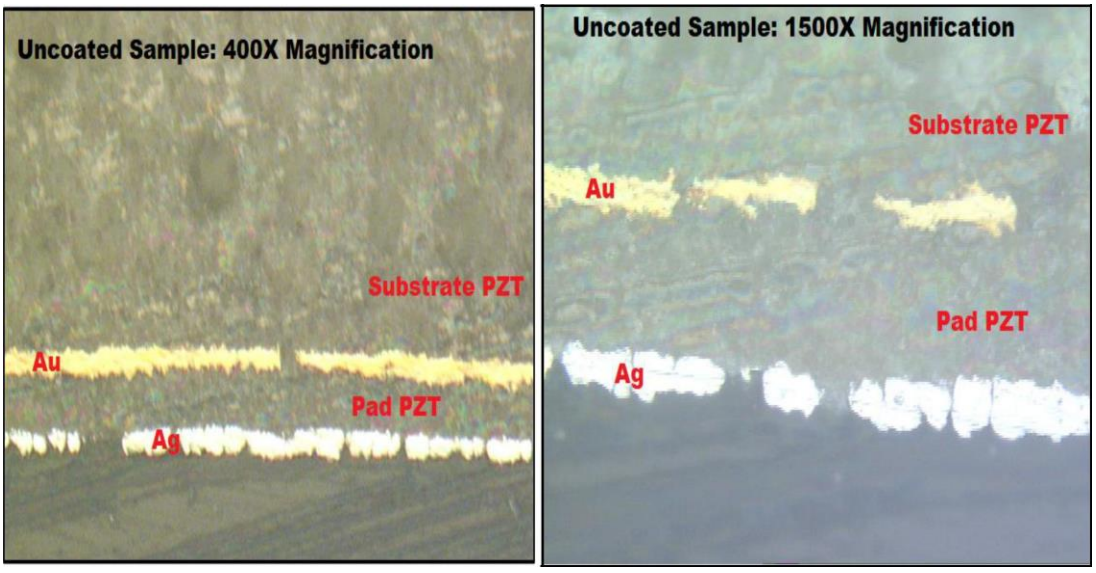

Figure 22. Optical microscopy image of uncoated sample.

Figure 23 shows the optical micrograph of coated sample; sample is coated with parylene, which over the Ag layer and not subjected to poling. Note, no visible discontinuities are observed in the Ag and Au layers. The comparison of the Figures 34 and 35 show lack of reproducibility of the electrode printing processes. The electrode layer discontinuities can be directly related to poor electromechanical properties and the observance of weak or no echo when subjected to electrical tests. Also, the electrode discontinuities may lead to Parylene migration into the pad and porous substrate layers (observed and described next), thereby diminishing the performance even further.

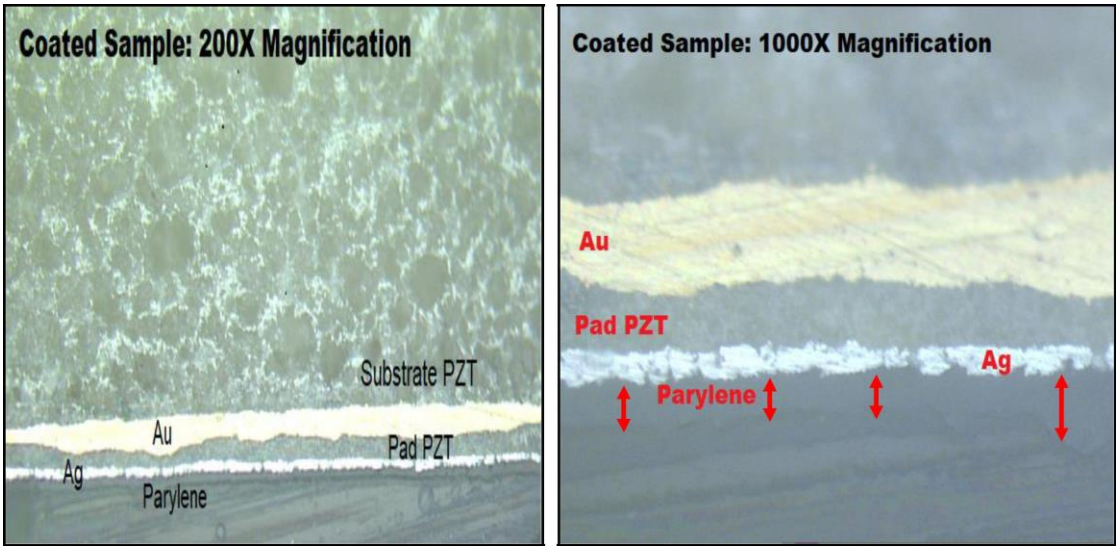

Figure 23. Optical microscopy image of coated sample.

Figures 24 and 25 shows SEM micrographs of fail-1 and operational-1 samples, respectively. The etched samples show open porosity clusters, non-uniformity in microstructure with respect to different phases (which causes defect pinning for domains). The presence of porosity clusters leads to areas in the pad where the material is not

piezoelectric, and such sites may restrict neighboring domain movements. Since the air in the large porosity clusters have different impedance compared to pad and electrodes, the mismatch is detrimental.

Figure 26 shows serious delamination of Au-substrate PZT and Ag-pad PZT in fail-2 sample and discontinuities in Ag, Au layers. Figure 27 shows discontinuities whereas no delamination observed in operational-2 sample. Delamination between layers changes the acoustic and electrical impedances leading to unforeseen behavior of the material and/or the failure of the device.

Table 10 shows the EDX data taken at different locations on operational sample (Figure 26). Table 11 shows the EDX data taken at different location on fail sample (Figure 27). Both the analyses show that there is no Ag migration into the surface and confirms the stacking composition as per the design.

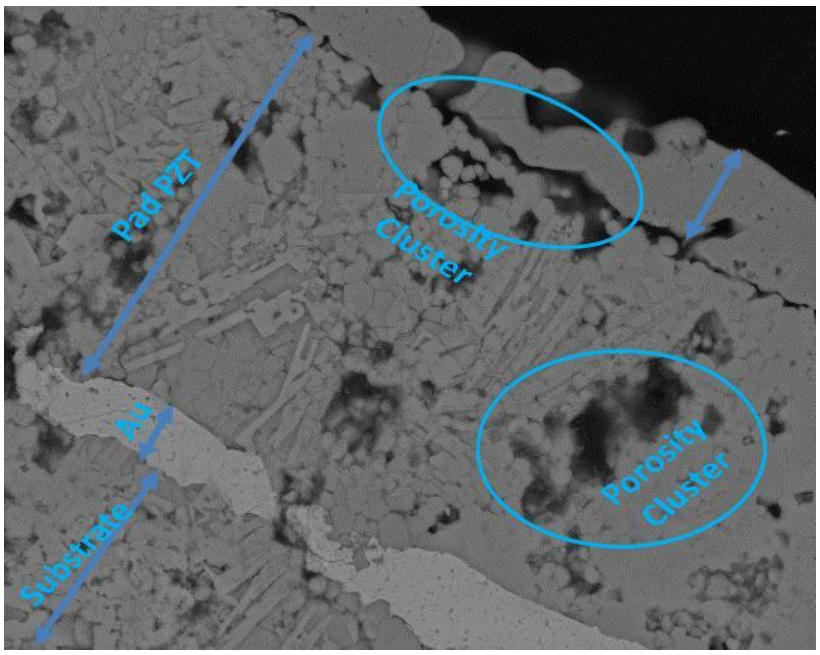

Figure 24. SEM image of fail-1 sample.

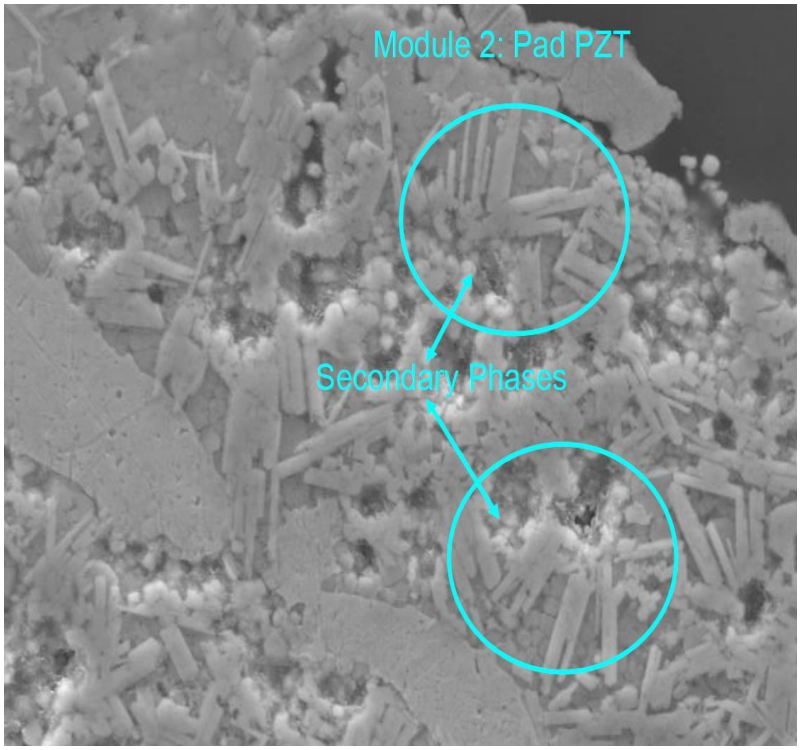

Figure 25. SEM image of operational-1 sample.

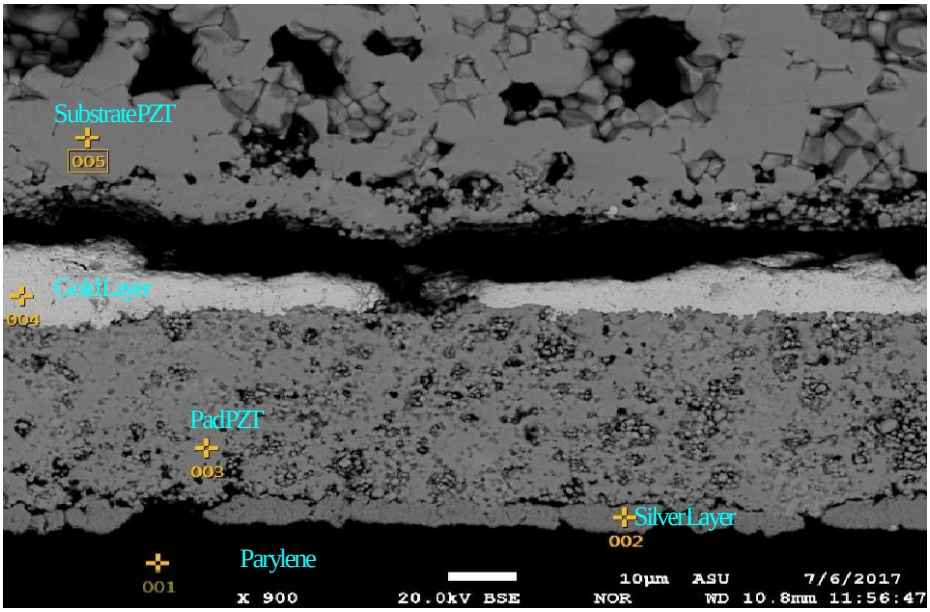

Figure 26. SEM image of fail-2 sample.

Table 10. EDX data of fail sample from Figure 26

Oxides	@ 001 (Parylene)	@002 (Ag)	@003 (Pad)	@004 (Au)	@005 (Substrate)
TiO_2	0	0.19	9.69	0	10.65
ZrO_2	0	0.75	16.78	0	18.18
Ag_2O	0	98.51	0.26	0	0.15
Sb_2O_3	0	0	0.74	0	0.5
PbO	0	0	72.53	0	70.52
C	88.36	0	0	0	0
Cl	11.35	0	0	0.05	0
Au_2O_3	0	0	0	99.95	0

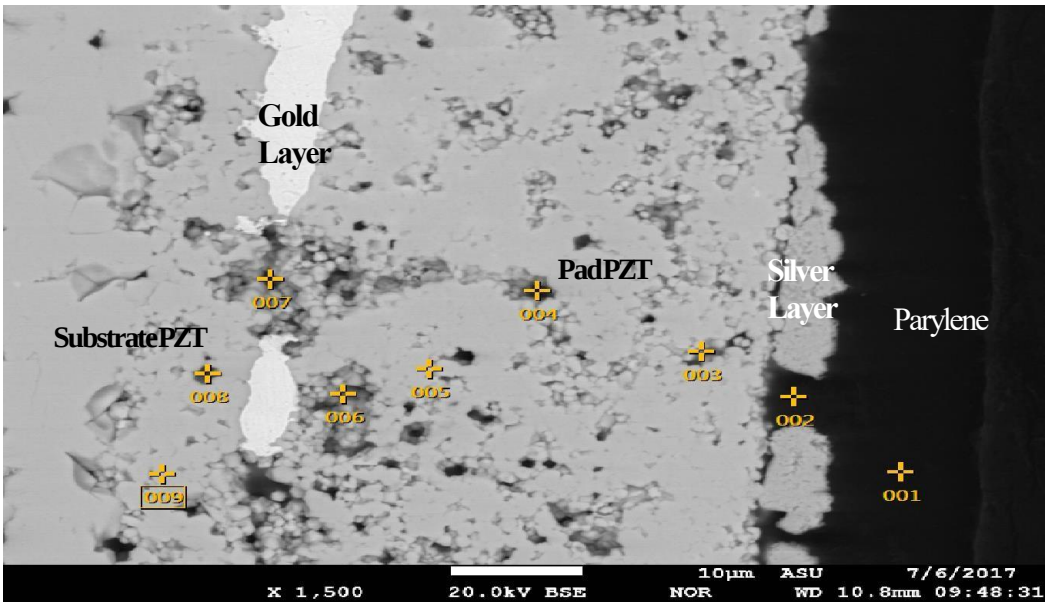

Figure 27. SEM image of operational-2 sample.

Table 11. EDX data of operational sample from Figure 27.

Oxides	@001 Parylene	@002 Ag	@003 Pad	@004 Pad	@005 Pad	@006 Pad	@007 Au	@008 Substrate	@009 Substrate
TiO_2	0	0.33	7.92	13.48	9.98	10.44	11.11	11.11	11.6
ZrO_2	0	0.82	10.86	11.29	16.4	12.68	17	17.6	17.08
Ag_2O	0	10.79	0	0	0	0	0	0	0
PbO	0	0	46.78	69.51	68.61	52.9	71.29	71.29	70.92
C	90.85	81.76	34.44	0	5	23.98	0	0	0
Cl	9.15	6.29	0	0	0	0	0	0	0
Au_2O_3	0	0	0	0	0	0	0	0	0
CuO	0	0	0	5.73	0	0	0.4	0	0.4

4.7 STEM/TEM:

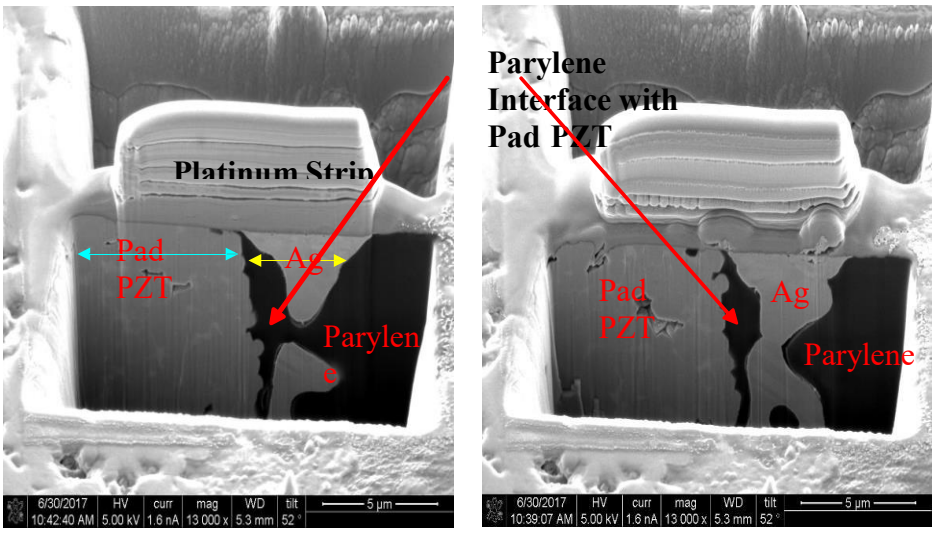

Figure 28. SEM image during FIB sample preparation of operational sample.

Figure 28 shows the SEM image of an operational sample during FIB lift-out procedure. The migration of polymer in to the Ag-Pad PZT interface is observed. This denotes that even though some samples have passed the electrical tests, there is high possibility of imminent failure.

Figure 29 are TEM images of operational samples showing the presence of complex ferroelastic and ferroelectric domains, and confirmation of poling and ferroelectricity on the received samples. Figure 30 shows the STEM-HAADF image of fail sample. The EDX spectrum inside the PZT area shows the presence of carbon and chlorine indicating that Parylene has migrated deep into the pad PZT. Figure 31 shows the STEM HAADF and BF image. The contrast in BF shows the presence of Parylene deep inside the pad PZT. Figure 32 shows TEM image of fail sample prepared by regular polishing and dimpling. The image shows dark areas (island) of Pad PZT (EDX spectrums c, d, e and f) and light areas of surrounding Parylene (EDX spectrums b and g).

The fail samples subjected to E-fields shows Parylene deep inside the pad layers. Since the glass transition temperature of Parylene (80ºC-100ºC) is low, the heat generated due to the electrical tests coupled with the discontinuities of the Ag layer allows the Parylene to flow by capillary action into the porous pad PZT layer. This causes further dilution of electrical, mechanical, and electromechanical properties of the PZT, which in turn directly influences the pulse echo sensitivity.

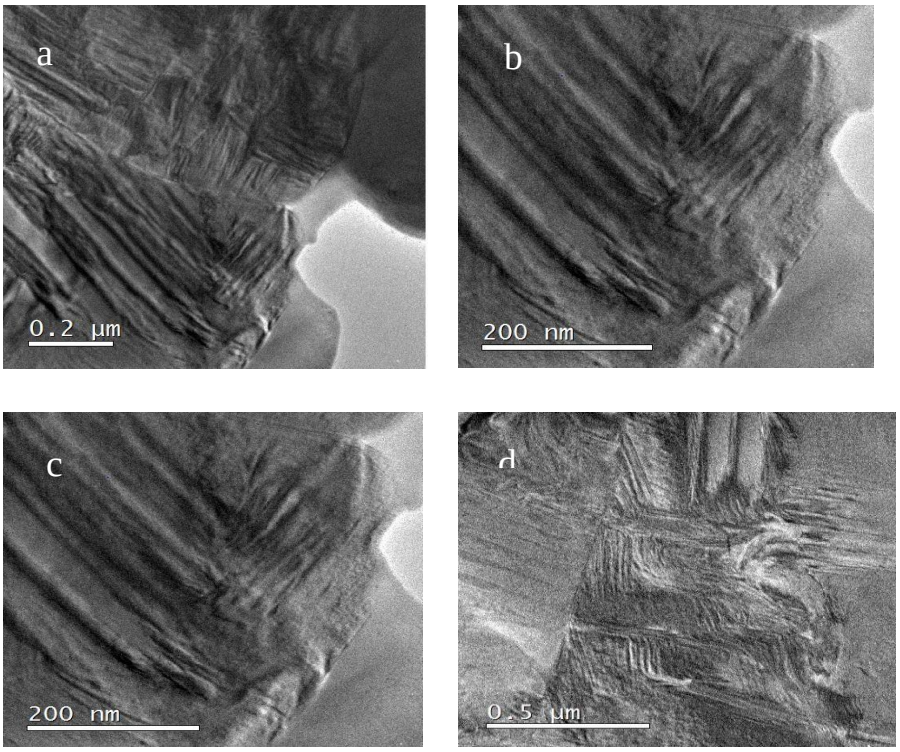

Figure 29. TEM images of operational sample.

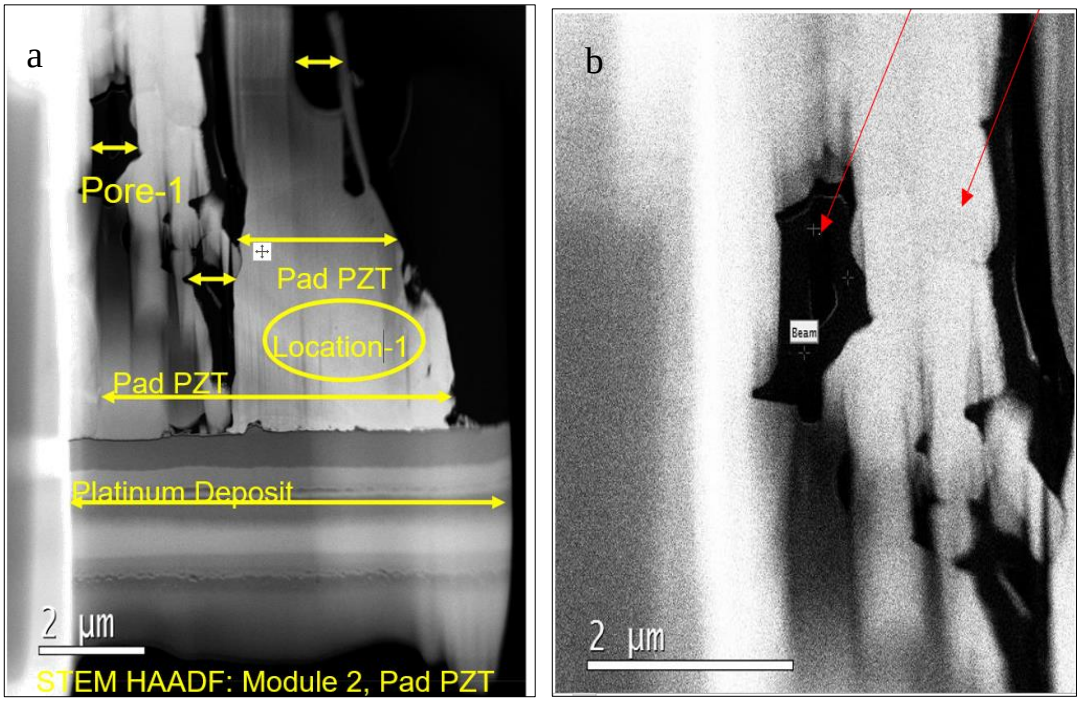

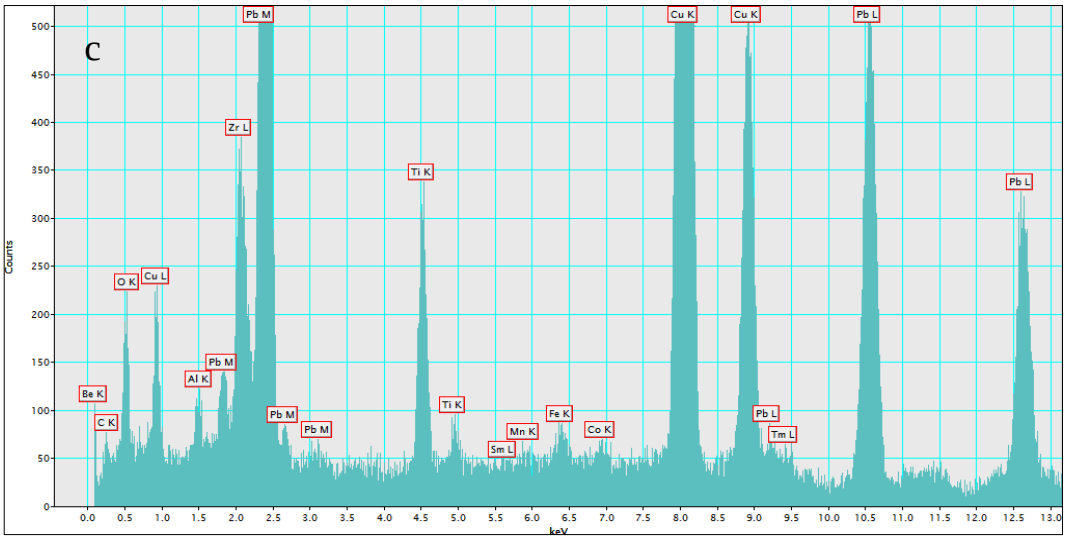

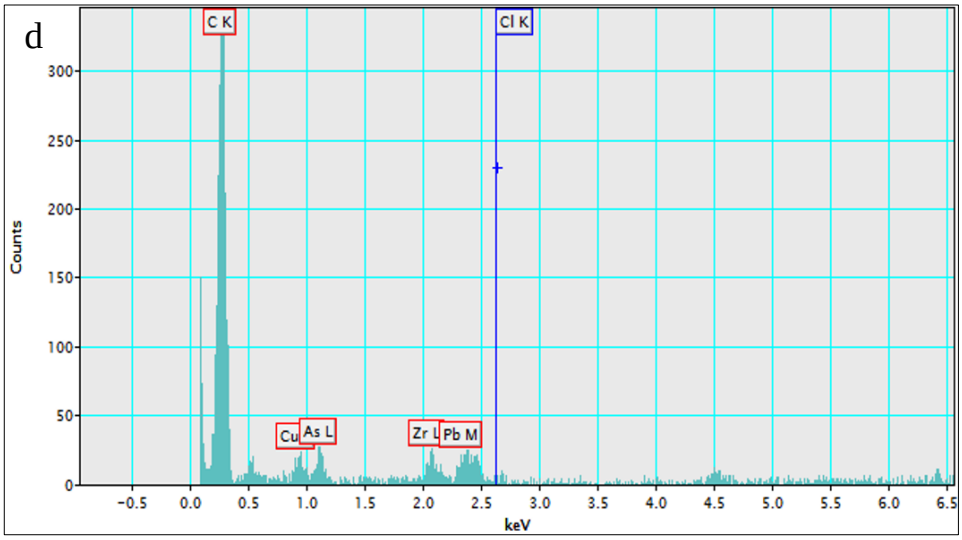

Figure 30. Fail (a) shows STEM-HAADF image of FIB made sample, (b) magnified image of pore, (c) EDX Spectrum from image (a); on PZT, (d) EDX Spectrum of (b); on pore.

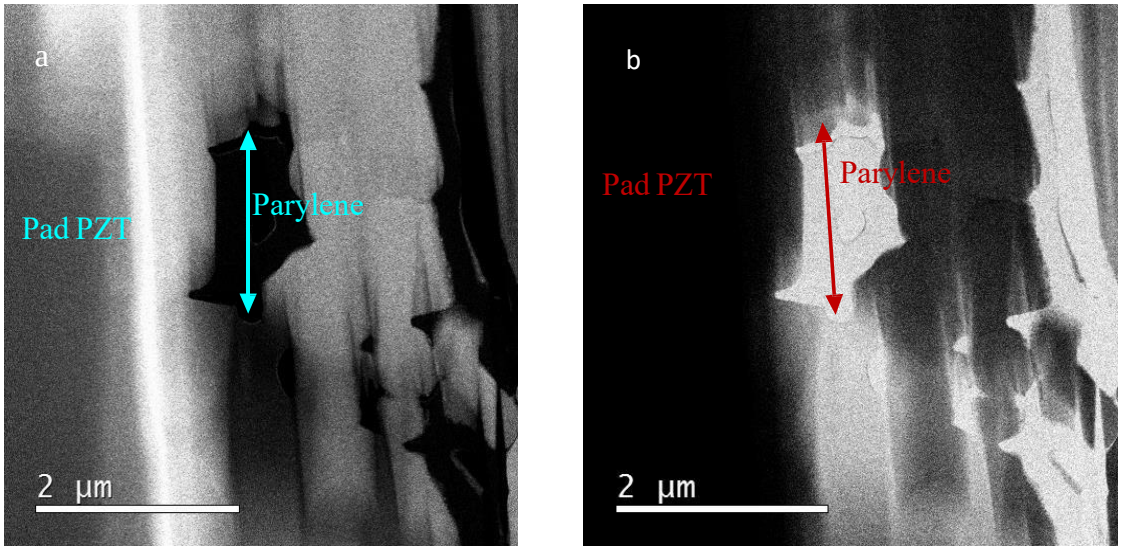

Figure 31. Fail sample: (a) STEM-HAADF image, (b) STEM-BF (bright field) image.

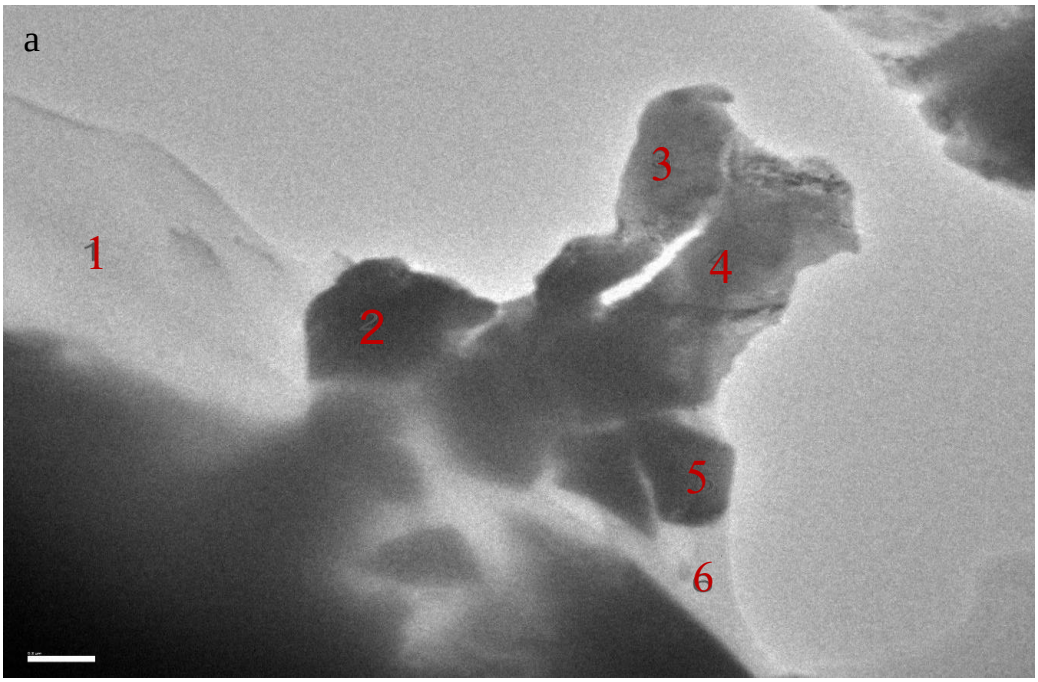

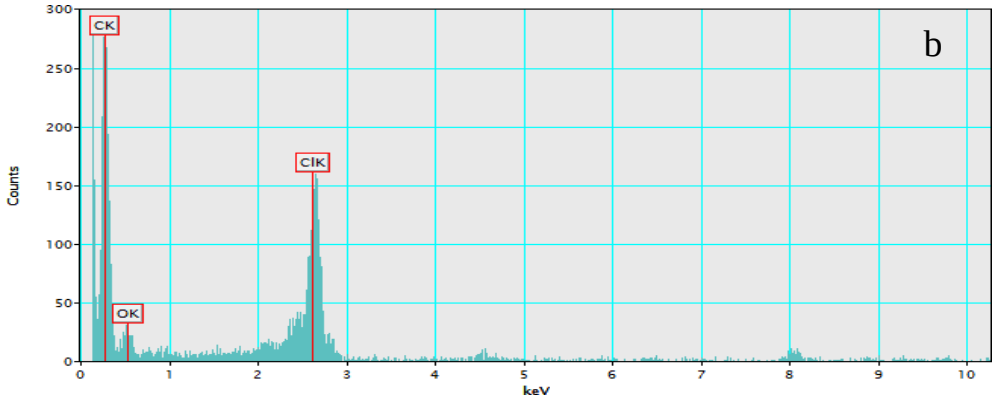
b
CK
OK
ClK
Counts
keV

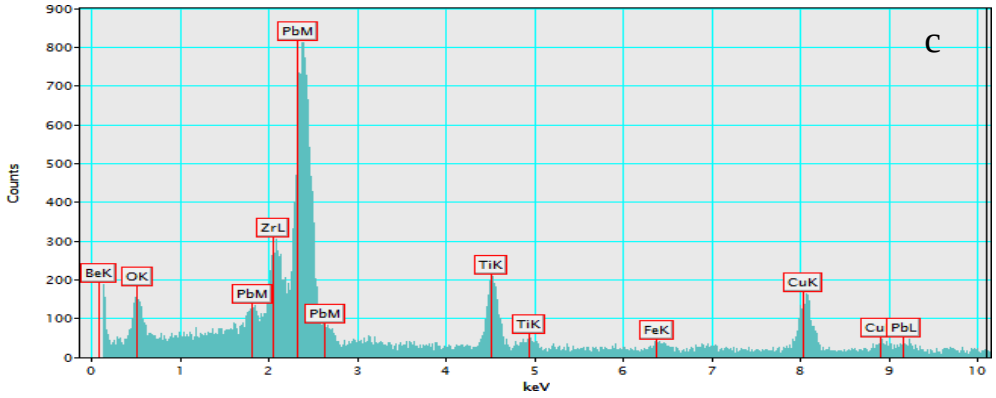
c
BeK
OK
PbM
ZrL
PbM
PbM
TiK
TiK
FeK
CuK
Cu
PbL
Counts
keV

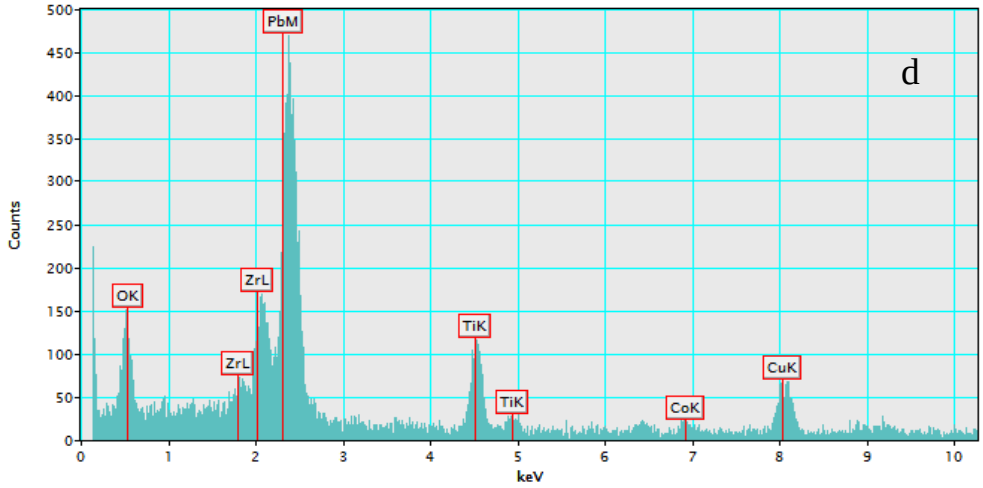
d
OK
ZrL
ZrL
PbM
TiK
TiK
CoK
CuK
Counts
keV

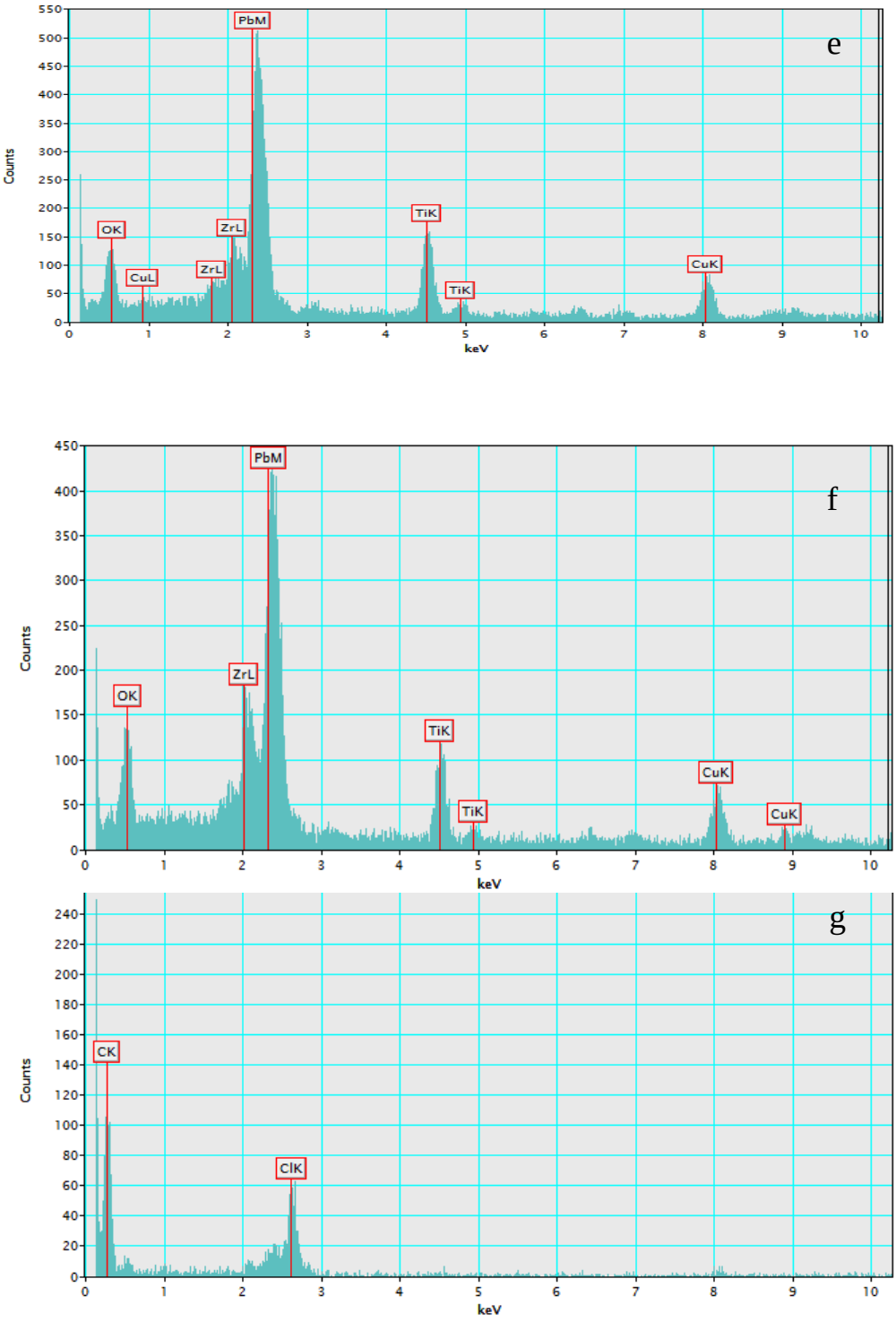

Figure 32. TEM image of fail sample and EDX spectrums from different locations on the sample.

CHAPTER 5

CONCLUSIONS

XRD:

1. All Pad samples exhibit both tetragonal and rhombohedral peaks.
2. Values for the tetragonal c/a ratio are constant for all samples and confirms with the value for MPB composition

DTA/TGA:

1. Consistent presence of peaks in all samples; incomplete calcination of material.

WDS:

1. Quantitative analysis of all samples shows the composition as Pb ($Zr_{0.52}$ $Ti_{0.48}$) O_3.
2. All pad samples have an excess of PbO.
3. Fail pad samples higher amount of excess PbO compared to operational samples.
4. Sb, Al and Mn elements detected in all pad samples are hard dopants.
5. Presence of Cu is due to the sintering aid (Cu_2O) used for reducing the sintering temperature.
6. All substrate samples show negligible amount of excess PbO.

Optical Microscopy:

1. Discontinuities in the Au and Ag layers are observed (Uncoated sample, not subjected to E-fields).
2. No discontinuities observed (Coated sample, not subjected to E-fields). This shows lack of reliability and reproducibility of the processes.

SEM:

1. Discontinuities and porosity clusters observed (Operational 1 sample).
2. Discontinuities, porosity clusters and predominant delamination observed (Fail 1 sample). Delamination in samples is an effect of E-fields.

STEM/TEM:

1. Presence of Parylene at Ag and pad (FIB Image).
2. Presence of Parylene deep inside the pad (HAADF image, Fail).
3. Dark areas (island) of Pad and light areas of surrounding Parylene observed (TEM image, Fail; deleterious effect of E-field).

Transducer Stack:

The final measured stack of the transducer is in the Figure 33.

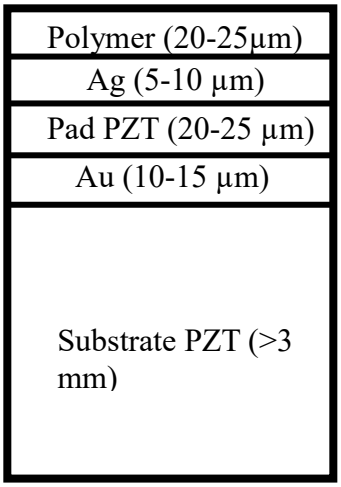

Figure 33. Transducer Stack.

REFERENCES

[1] C. R. W. Bernard, Jaffe, Jaffe Hans, *Piezoelectric Ceramics*. Academic Press Inc., 1971.

[2] E. Filoux, R. Lou-Moeller, S. Callé, M. Lethiecq, and F. Levassort, "Optimised properties of high frequency transducers based on curved piezoelectric thick films obtained by pad printing process," *Adv. Appl. Ceram.*, vol. 112, no. 2, pp. 75–78, 2013.

[3] T. R. Gururaja, "Piezoelectric transducers for medical ultrasonic imaging," *IEEE Int. Symp. Appl. Ferroelectr.*, pp. 259–265, 1992.

[4] J. M. Cannata, T. A. Ritter, W. H. Chen, R. H. Silverman, and K. K. Shung, "Design of efficient, broadband single-element (20-80 MHz) ultrasonic transducers for medical imaging applications," *IEEE Trans. Ultrason. Ferroelectr. Freq. Control*, vol. 50, no. 11, pp. 1548–1557, 2003.

[5] M. Hagh, "25 MHz Ultrasonic Transducers with Lead- Elements," *Elements*, vol. 56, no. 2, pp. 368–378, 2009.

[6] K. Uchino, *Advanced Piezoelectric Materials: Science and Technology*, 2nd ed. Woodhead Publishing Series.

[7] (f) J. C. Burfoot and G. W. Taylor Taylor, *Polar Dielectrics and their Applications*. Macmillan.

[8] S. E. Park and T. R. Shrout, "Characteristics of relaxor-based piezoelectric single crystals for ultrasonic transducers," *IEEE Trans. Ultrason. Ferroelectr. Freq. Control*, vol. 44, no. 5, pp. 1140–1147, 1997.

[9] W. A. Smith, "The role of piezocomposites in ultrasonic transducers," *Proceedings., IEEE Ultrason. Symp.*, pp. 755–766, 1989.

[10] S. Priya and S. Nahm, *Lead-free piezoelectrics*. 2011.

[11] K. Uchino, "Advanced Piezoelectric Materials: Science and Technology," 2010.

[12] D. Waller and J. Chen, "Requirements of piezoelectric materials for medical ultrasound transducers," *Appl. Ferroelectr.*, pp. 565–568, 1996.

[13] R. E. N. and G. R. Ruschau, *Smart Electroceramics*.

[14] A. J. Moulson, *Electroceramics: Materials, Properties, Applications*. Chapman &

Hall.

[15] “Navy Type PZT Classifications | Sensor Technology Ltd.” [Online]. Available: https://sensortechcanada.com/technical-notes/articles/navy-type-pzt/. [Accessed: 30-Jul-2018].

[16] R. J. D. Tilley, *Understanding Solids*. 2004.

[17] M. Kimura, A. Ando, and Y. Sakabe, “Lead zirconate titanate-based piezo-ceramics,” *Adv. Piezoelectric Mater. Sci. Technol.*, pp. 89–110, 2010.

[18] K. Roleder, D. Grzywacz, and J. Wolak, *Time dependent properties of PbZr x Ti 1-x O 3 crystals*, vol. 124, no. 1. 1991.

[19] K. Uchino, “Introduction to Piezoelectric Actuators and Transducers Kenji Uchino , International Center for Actuators and Transducers , Penn State University,” no. 5, p. 40, 2003.

[20] P. K. Panda and B. Sahoo, “PZT to lead free piezo ceramics: A review,” *Ferroelectrics*, vol. 474, no. 1, pp. 128–143, 2015.

[21] H. Debéda, C. Lucat, M. Maglione, V. Pommier-Budinger, X. Hochart, and W. Sourbe, “Feasibility of screen-printed PZT microceramics for structural health monitoring applications,” *Int. J. Appl. Ceram. Technol.*, vol. 11, no. 3, pp. 413–421, 2014.

[22] M. Lethiecq *et al.*, “Non-planar pad-printed thick-film focused high-frequency ultrasonic transducers for imaging and therapeutic applications,” *IEEE Trans. Ultrason. Ferroelectr. Freq. Control*, vol. 59, no. 9, pp. 1976–1982, 2012.

[23] M. Fink, “(z = 30.10",” pp. 611–614, 1991.

[24] A. Guiroy *et al.*, “Dual-frequency transducer for nonlinear contrast agent imaging,” *IEEE Trans. Ultrason. Ferroelectr. Freq. Control*, vol. 60, no. 12, pp. 2634–2644, 2013.

[25] F. Levassort, M. Lethiecq, and E. Filoux, “P3Q-3 Curved Piezoelectric Thick Films for High Resolution Medical Imaging,” *2006 IEEE Ultrason. Symp.*, pp. 2361–2364, 2006.

[26] “Powder X-ray diffractometer (Bruker D8) | Eyring Materials Center.” [Online]. Available: https://le-csss.asu.edu/equipment/powder-x-ray-diffractometer-bruker-d8. [Accessed: 06-Jul-2018].

[27] “Calorimetry (TGA/DTA/DSC) | Eyring Materials Center.” [Online]. Available: https://le-csss.asu.edu/equipment/calorimetry. [Accessed: 06-Jul-2018].

[28] Alan Koenig, “Denver Inclusion Analysis Laboratory - Instruments - LA-ICPMS.” [Online]. Available: https://minerals.cr.usgs.gov/dial/LA_ICPMS.html. [Accessed: 06-Jul-2018].

[29] “University of Arizona Electron Microprobe Lab EPMA Intro.” [Online]. Available: http://pirlwww.lpl.arizona.edu/~domanik/UA_Microprobe/Intro.html. [Accessed: 06-Jul-2018].

[30] “X-ray Photoelectron Spectroscopy (VG 220i-XL) | Eyring Materials Center.” [Online]. Available: https://le-csss.asu.edu/equipment/x-ray-photoelectron-spectroscopy-vg-220i-xl. [Accessed: 06-Jul-2018].

[31] Axel Wittman, “Electron Microprobe | Eyring Materials Center.” [Online]. Available: https://le-csss.asu.edu/equipment/electron-microprobe. [Accessed: 06-Jul-2018].

[32] “CM200-FEG (Philips) | Eyring Materials Center.” [Online]. Available: https://le-csss.asu.edu/equipment/cm200-feg-philips. [Accessed: 06-Jul-2018].

[33] “ARM200F (JEOL) | Eyring Materials Center.” [Online]. Available: https://le-csss.asu.edu/equipment/arm200f-jeol. [Accessed: 06-Jul-2018].

[34] “FIB & Sample Prep | Eyring Materials Center.” [Online]. Available: https://le-csss.asu.edu/techniques/fib-sample-prep. [Accessed: 06-Jul-2018].

[35] B. Noheda, D. E. Cox, G. Shirane, R. Guo, B. Jones, and L. E. Cross, “Stability of the monoclinic phase in the ferroelectric perovskite PbZrr1-xTixO3,” *Phys. Rev. B - Condens. Matter Mater. Phys.*, vol. 63, no. 1, pp. 1–8, 2001.